

## The NTUGCM's AMIP Simulation on the East Asian Summer Monsoon

Wen-Shung Kau<sup>1</sup>

(Manuscript received 6 November 1997, in final form 16 March 1998)

### ABSTRACT

The Asian summer monsoon accompanies two systems, the Indian monsoon and the East Asian monsoon. A major difference between the Asian and the Indian monsoon is that beginning in early May, the Asian monsoon takes about two months, to migrate over an extensive area from southern to northern China. At the same time, the associated heavy rainfall also moves from south to north. The monsoon rain-band associated with the Indian monsoon takes only one to two weeks to migrate from Southern to Northern India. The onset of the Southeast Asian southwest monsoon initiates the East Asian monsoon (EASM).

Based on the NMC global spectral model, with significant modifications to virtually all of the physical parameters, we have developed a general circulation atmospheric model i.e. NTUGCM. The NTUGCM was used to perform an AMIP integration from 1 January 1979 to 31 December 1988. For the JJA (June, July, August) climatology, the simulated stream function at 850 hPa captures most of the major features in the observed climatological-mean fields. *e.g.*, the subtropical high over the ocean, the cyclonic circulation over South Asia and the eddy straddling the equator in the Indian Ocean, as well as the Tibetan high, simulated in the 200 hPa stream function. In general, the NTUGCM gives a better simulation at 850 hPa than at 200 hPa and a better simulation around a large forcing region, *e.g.* South Asia, than around a weak forcing region, *e.g.* the Eastern Pacific and South American coast. The best simulation for precipitation is found in the Asian monsoon region where maximum precipitation occurs.

The EASM rainfall distribution is the result of complex interactions between the atmosphere, the earth's surface and the tropical and extra tropical systems. The EASM rainfall distribution involves a wide range of spatial and temporal scales from the mesoscale to the planetary scale. The NTUGCM is able to simulate the large scale features of the EASM and the sudden change of the monsoon rainfall which is associated with abrupt changes in large scale atmospheric circulation. This study also analyzes the onset characteristics of the EASM simulated by the model. The AMIP simu-

---

<sup>1</sup>Department of Atmosphere Sciences, National Taiwan University, Taipei, Taiwan, ROC

lation of the NTUGCM gives the onset date of the EASM as 13 May.

The present results are encouraging, however, there are still many obvious issues that remain to be studied, such as the linkage between the monsoon's variation and surface boundaries forcing, the cause of the seasonal northward jump of the subtropical high, the dynamic and thermodynamic effects of the Tibetan Plateau and an improved model representing the physical parameters.

(Key words: AMIP, NTUGCM, East Asian summer monsoon, Indian monsoon, Subtropical high, Surface boundary forcing)

## 1. INTRODUCTION

Climate is an extraordinarily complex environmental system. In the study of the many processes responsible for a given climate's structure and variation, the atmospheric scientist has found it is necessary to construct mathematical models of the climate in order to represent quantitatively the various interacting elements. In addition to the atmosphere, the scientific definition of climate also includes the average behavior of the oceans and the condition or state of the land surface and its associated vegetation. Each of these elements are linked together in a worldwide system, with changes in one part generally affecting the behavior of other parts, setting in motion a chain of events which may either reinforce or cancel the original change. The number of possible mechanisms causing changes in climate are rather large. Our knowledge of the physical basis of climate and climate variation is most usefully and comprehensively organized in terms of models, which are mathematical representations of the physical laws and govern the climate system's behavior. From such models the system's future behavior or climatic state may then in principle be determined. In this sense, climate models represent the most physically rational basis for studying climate. The general circulation model (GCM) has been used extensively to study both global climate changes and observed regional climate characteristics. A comparison of simulated and observed seasonal variations for the monsoon system can therefore contribute substantially to the evaluation and improvement of the inter-annual variability of the GCM model and lead to an understanding of short term climate variations. In this research we have focused on the GCM's simulation of the East Asian summer monsoon.

The monsoon is a part of the seasonal variations caused by the annual variation in solar fluxes to the earth's surface. Although convective heating plays the most dominant role as a driving force for monsoon circulation (*e.g.* Krishnamurti and Ramanathan, 1982), the land-ocean heat contrast caused by the seasonal variations in solar radiation provides a basic framework for the large-scale monsoon circulation. If inter-annual variations in large scale monsoon circulation are determined entirely by lower boundary forces, they could, in principle, be simulated perfectly by the GCM, integrated with specified observed lower boundary conditions. On the other hand, it is possible that nonlinear internal atmospheric dynamics, being most powerful on intra-seasonal time scales, could limit monsoon predictability on inter-annual

time scales. Therefore, using the GCM model to simulate monsoon circulation is a good approach to verify the climate model's capability.

Yanai *et al.* (1992) carefully analyzed the FGGE data and concluded that there are two transition phases to the Asian summer monsoon (ASM) in the early summer. The first transition is marked by the onset of the East Asian summer monsoon (EASM), while the second transition is marked by the onset of the Indian summer monsoon (ISM). Nakazawa (1992) examined the climatological mean evolution of the ASM, and found the same characteristics. Climatically, the first transition occurs around 11-15 May and is characterized by the establishment of a southwesterly flow at 850 hPa over the longitudes east of 80° E, covering the Bay of Bengal, Indochina and the South China Sea (SCS). Enhanced precipitation spreads over the west coast of the Malay Peninsula, Indochina and SCS. It also coincides with the beginning of the Mei-Yu season in Taiwan. The second transition occurs about 2-3 weeks later around the 5-9 of June, during which the southwesterly winds over the Arabian Sea develop and heavy rains commence at the southwestern tip of India. At about the same time the Mei-Yu starts in the Yangtze River Valley. Atmospheric circulation during the first transition fluctuates in a more regional scale. In contrast, the circulation during the second transition fluctuates on a much larger spatial scale (Hsu & Chen, 1997). The EASM rain band is typically a quasi-stationary large-scale feature that produces continuous precipitation. Embedded within the rain band are mesoscale vortices which produce intense local rainfall. In the EASM system there are two rain belts. One is linked to a monsoon trough in the SCS and the ITCZ in the Western Pacific and has a tropical nature. The other rain belt is formed through the joint contribution of a cold air mass from the polar continent and a warm and wet flow from the north side of the subtropical high (SH). This rain belt is known as the Mei-Yu and it has a subtropical nature.

The EASM rain band takes about two months, from early May, to spread over an extensive area from Southern to Northern China. In the Indian Monsoon system, there is only one rain belt corresponding to the monsoon trough which is of a tropical nature, and it takes only about one to two weeks to migrate from Southern to Northern India. The establishment of the EASM over the SCS depends on the equatorial westerly wind near 70-90° E, or the southwesterly flow which may come from the south side of the SH and turn to a southwesterly direction on the west side of the SH and northwest side of the SH. However, the onset of the ISM relies on the cross-equatorial flow near 40° E. Therefore, the EASM cannot be simply viewed as northward and eastward extensions of the Indian summer monsoonal flow. According to a suggestion by Tao (1985), the principal components of the EASM should include: the monsoon trough (or ITCZ) in the SCS and the Western Pacific, the cross-equatorial flow to the region east of 100° E, the SH over the Western Pacific, the upper-level easterly flow, the convection along the monsoon trough, the Mei-Yu frontal zones and the mid-latitude disturbances. The principal components of the ISM system suggested by Krishnamurti & Bahalme (1976) include: the monsoon trough over Northern India, the southwest monsoon flow, the cross-equatorial flow, the Somali jet off East Africa, the Mascarene high, the anticyclone in the upper troposphere over the Tibetan Plateau, the tropical easterly jet stream and monsoon rainfall and the cloud cover over the Indian Peninsula. Therefore, the EASM is influenced not only by the Indian monsoon, but also by the Western Pacific SH. Because of large

inter-annual and inter-seasonal variations in the Western Pacific SH, the anomalies of summer monsoon rainfall and circulation are large in East Asia. Comparatively, the EASM is much more complicated and variable than the ISM.

There have been a lot of numerical experiments conducted by different modeling groups with their GCMs to study some aspects of the ASM ( Hahn & Manabe, 1975; Shukla, 1975; Washington *et al.*, 1977; Gilchrist, 1981; Sud and Smith, 1985; Kitoh and Tokioka, 1987; Yamazaki, 1988; Barnett *et al.*, 1989; Tibadi *et al.*, 1990; Bhaskar Rao *et al.*, 1991; Kitoh, 1992; Palmer *et al.*, 1992; Sperber *et al.*, 1994; Zewiers, 1993; Meehl, 1994; Yang and Lau, 1996). There is also active monsoon climate research in a numbers of institutes and universities in association with the Atmospheric Model Inter- comparison Project ( AMIP ), a coordinated effort to simulate the 1979-1988 decade using the observed monthly sea surface temperature(SST) from 1979 to 1988 with approximately 30 atmospheric GCMs (Gates 1992). However, the above studies emphasize the simulation of the ISM and pay little attention to the EASM.

In this paper, we show the recent AMIP simulation of the NTU (National Taiwan University) GCM on the EASM. Concerning the onset and progression of the EASM , some of the most important features from the climatological analysis and the NTUGCM simulation will be presented. In this report, section 2 provides a brief description of the dynamics and physics used in the NTUGCM. A short section follows the model description on the model climatology of JJA (section 3). A range of important climate variables produced by the model over a 10- year AMIP run is presented. Section 4 is the simulated EASM where the observed fields are displayed for comparison. Section 5 provides a summary and conclusion.

## **2. MODEL STRUCTURE**

The present NTU model, designed especially for simulation of the Asian monsoon, is based on the early NMC global spectral model described by Sela (1980). Subsequent changes include the substitution of a triangular truncation scheme for the model's original rhomboidal representation as well as significant modifications of virtually all of the physical parameterizations. Like most of the numerical weather prediction models, the climate model of the NTUGCM is based on primitive equations. The model simulates a comprehensive range of physical processes including radiation and precipitation, which act as forces on the dynamic equations.

### **2.1 Numerical and Computational Properties**

Because of the complexity of the model equations, realistic solutions can be obtained only through numerical simulations. For convenience, we consider the numerical methods in three parts: horizontal, vertical and time.

#### **2.1.1 Horizontal**

The horizontal representation of the model is spectral with transformation to a Gaussian grid for calculation of nonlinear quantities and physical processes. The present model has

been coded for variable spectral resolution. However, in this study we used the spectral triangular 42 (T42), roughly equivalent in to a grid spacing of 2.8 X 2.8 degrees.

### 2.1.2 Vertical

The vertical domain for the present model is from surface to 1hPa. For a surface pressure of 1000hPa, the lowest atmospheric level is 962hPa. Finite-difference sigma vertical coordinates with specification of layer locations after Brown (1974) and Phillips (1975) are adopted. The Quadratically conserving vertical finite-difference approximations of Arakawa and Mintz (1974) are utilized. There are 13 irregularly spaced sigma levels. For a surface pressure of 1000hPa, 3 levels are below 800hPa and 4 levels are above 200hPa (Figure 1).

### 2.1.3 Time integration

The time integration was accomplished using the so-called semi-implicit method by Robert (1969) with a moderate time filter. The time step is 20 minutes for dynamics and physics, while the radiation /cloud calculations were done once every 3 hours. The operating system for the present model was run on a DEC-3000/600 computer using a single processor in a UNIX environment. It took about 8 minutes of CPU time per simulated day for the AMIP simulation.

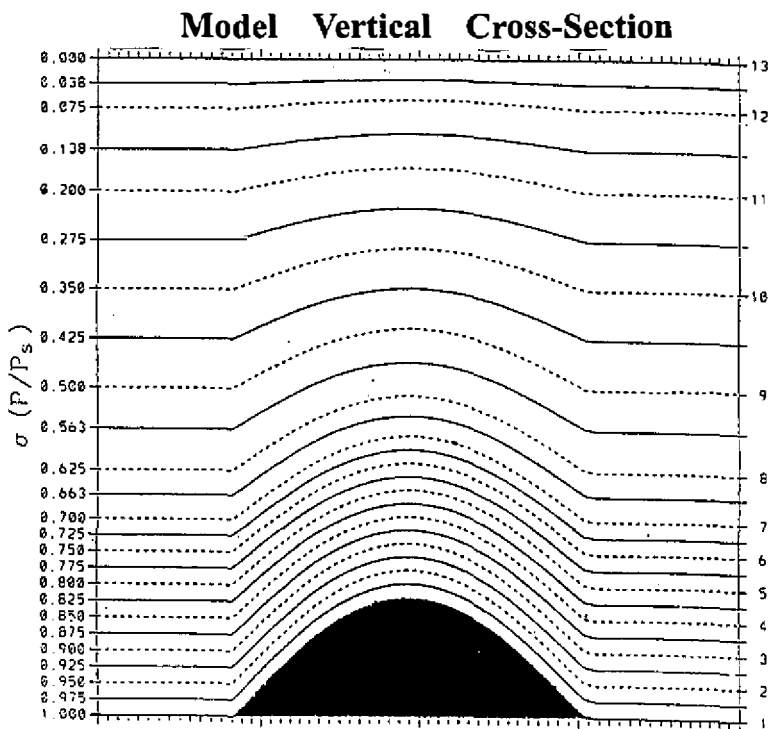


Fig. 1. Vertical structure of NTUGCM.

## 2.2 Dynamic and Physical Properties

The primitive-equation dynamics are expressed in terms of vorticity, divergence, temperature, specific humidity and the logarithm of surface pressure. Horizontal diffusion was applied to the temperature, vorticity, divergence and moisture fields. The diffusion is represented in a simplified spectral form based on Laursen and Eliassen (1989), where the diffusion coefficient varies for different variables and levels. The gravity wave drag parameterization by Chouinard *et al.* (1986) was included in the model, where the momentum transports due to the sub-grid scale gravity waves excited by stable stratified flow over irregular terrain were parameterized. For the atmospheric chemistry, carbon dioxide concentrations were at the AMIP-prescribed value of 345ppm and the monthly mean zonal averaged climatological ozone mixing ratios were specified as a function of latitude and height using data from Rosenfield *et al.* (1987).

The determination for the land or sea category of surface type was made from NCAR's 10 minute by 10 minute Navy topography dataset, which included the percentage of water-cover at any point. The data was averaged to the model's grid points. Any grid-box whose average water percentage was 60% or more was defined as a water point. The spatially variable surface albedo was prescribed by the climate data obtained from the Central Weather Bureau. Over oceans the albedo is specified as 0.09 and over ice 0.60. Monthly mean values were linearly interpolated to the current time. Surface orographic heights were determined by averaging the Navy 10 by 10 minute data over each model grid box. The averaged orography was then passed through a Lanczos (1966) filter. The model physics were formulated in a simplified parametric form. There are:

### 2.2.1 Radiation

The radiation transfer parameterization scheme is based on the broadband methods developed by Ou and Liou (1988), which calculated the transfer of infrared and solar fluxes in both clear and cloudy regions. In a clear atmosphere, the entire infrared spectrum is divided into five bands; three for water vapor, one for carbon dioxide and one for ozone absorption. The parameterization of these broadband infrared emissivities follow Liou and Ou (1981) and Ou and Liou (1988). The solar spectrum consists of 25 bands- six for water vapor, one for carbon dioxide (which overlaps the 2.7 micron band for water vapor) and 18 for ozone. The parameterization of the corresponding broadband solar absorptivities was documented by Liou *et al.* (1984).

In a cloudy atmosphere, low and middle clouds are treated as black bodies in the infrared radiation transfer calculation. The broadband infrared emissivity, reflectivity and transitivity for high clouds as well as broadband solar absorption, reflection and transmission for various cloud types are computed based on a prescribed vertical liquid water content. Cloud radiative properties were calculated based on the parameterizations developed by Liou and Wittman (1979). For purposes of the radiation calculations, clouds were assumed to be randomly overlapped in the vertical (Kau *et al.* 1995).

### 2.2.2 Convection

The parameterization of convection follows the approach of Kuo (1965) as adapted by Phillips (1979). Penetrative convection occurs in the presence of large moisture convergence accompanied by a moist unstable lapse rate under conditions of moderately high relative humidity. The convective cloud is assumed to dissolve instantaneously through a lateral boundary, thereby imparting heat and moisture into the environment. In a vertical column, the total moisture available from convergence is divided between a fraction  $b$  that moistens the environment and the remainder  $(1-b)$  that contributes to the latent heating (precipitation) rate. The moistening parameter  $b$  is prescribed as a function of the SST, i.e., the  $b$  value linearly decreases to zero by a factor when the SST is between 296 K to 299 K and is set to zero when the SST is equal to or greater than 299 K (Kau *et al.*, 1995).

### 2.2.3 Cloud formation

The cloud cover and liquid water content required for the radiation calculations were determined diagnostically following Gelyn (1981), Liou and Zheng (1984), and Slingo and Ritter (1985). This scheme is based on whether the ambient relative humidity exceeds prescribed threshold values (Gelyn, 1981). The amount of cloud is a quadratic function of the excess relative humidity. The model allows partial or total cloud cover in seven vertical sigma layers (layers 3 to 9), while the top two layers and the bottom three layers are specified as being cloudless (i.e. no stratiform cloud below 850 hpa). The model-generated multi-layered cloudiness is then placed into high, middle and low cloud decks (Kau *et al.*, 1995).

### 2.2.4 Precipitation

Precipitation can result either from convection or from large-scale condensation, when the local specific humidity exceeds the saturated humidity at the environmental temperature/pressure. Evaporation of convective precipitation is parameterized as a function of convective rain intensity and saturation deficit. Before falling to the surface, large-scale precipitation must saturate all layers below the condensation level by evaporation. Precipitation that reaches the surface is assumed to be uniformly distributed over a grid box.

### 2.2.5 Planetary boundary layer(PBL)

The PBL top is defined as the lifting condensation level and is assumed at the lowest model layer. The surface wind velocity was determined using the parameterizations of the Drag Law. The surface temperature over land is calculated from the surface heat budget equation (Liou and Zheng, 1984) using a force-restore method. The surface fluxes are computed, using the bulk aerodynamic method, to a diffusive flux from the surface layer into the layer above. Three mechanisms are considered in terms of fluxes into the atmosphere: surface friction, sensible heat fluxes from the surface, and the evaporation from the surface (moisture

flux) are expressed as a bulk formula. The values of wind, temperature and humidity required for the bulk formula were taken to be those at the lowest atmospheric level, which was assumed to be within a constant-flux surface layer. The drag coefficients for surface stress vary geographically from a minimum of 0.0013 over the open oceans to a maximum of 0.009 over the Himalayas. Thermal and moisture drag coefficients are the same and allow the transfer process to be highly wind speed selective (Sela, 1980).

### 3. MODEL CLIMATOLOGY OF JJA

The NTUGCM was used to perform an AMIP integration from 1 January 1979 to 31 December 1988. SST was prescribed to force the model. Two kinds of SST temporal means were used—a sequence of 36 monthly SSTs taken between 1979 and 1981, and 366 sequences of weekly SSTs between 1982 and 1988. The initial condition was the circulation of 31 December 1978, which was taken from the ECMWF FGGE data set. In this section, we describe the model climatology of JJA. The following two sets of observed data were used for model verification: ( a ) the general circulation statistics derived from the climatology of the ECMWF analysis for 1985-1995;( b ) Legates/MSU precipitation climatology produced by Wallace *et al.* ( 1994, personal communication ).

#### 3.1 Zonal Means

Cross- sections of the zonal-averaged zonal winds are shown in Figure 2. On the whole, the location and strength of the simulated jets in the extra-tropics of the Northern and Southern Hemispheres are quite similar to the observed. The polar night jet in the Southern Hemisphere was also simulated. However, the tropical easterly flow in the model is too weak in the middle troposphere. Figure 3 shows cross sections of the zonal-averaged temperature. In general the simulated zonal-averaged temperature agrees with the observation. The model bias indicates that in the tropics, the lower troposphere is colder(these results are very similar to ECHAM0(Dumenil and Schlesse , 1987)).This error is caused primarily by a lack of latent heat exchange between the ocean surface and the atmosphere , predominately in the tropical Pacific. Another contributing factor might be the excessive radiative cooling caused by tropical cirrus cloud (Roeckner *et al.* , 1989). The zonal averaged meridional wind and vertical velocity are shown in Figures 4 and 5, respectively. From these figures we see that the basic structure of the zonal mean Hadley and Ferrel cells are simulated . However , the upper tropospheric wind peak is too weak , suggesting a deficiency in the convection scheme . This feature is also consistent with the vertical structure of the temperature errors as shown in Figure3.

#### 3.2 Global Projections

Simulated stream function and zonal winds at 850hPa are shown in Figure 6. The model captures most of the major features in the observed climatological mean fields, *e.g.* the SH over the oceans, the cyclonic circulation over South Asia and the eddy straddling the equator in the Indian Ocean. However, the circulation appears to be more zonal than the observed, suggesting weaker amplitudes for the stationary eddies. The SHs in the Northern Hemisphere

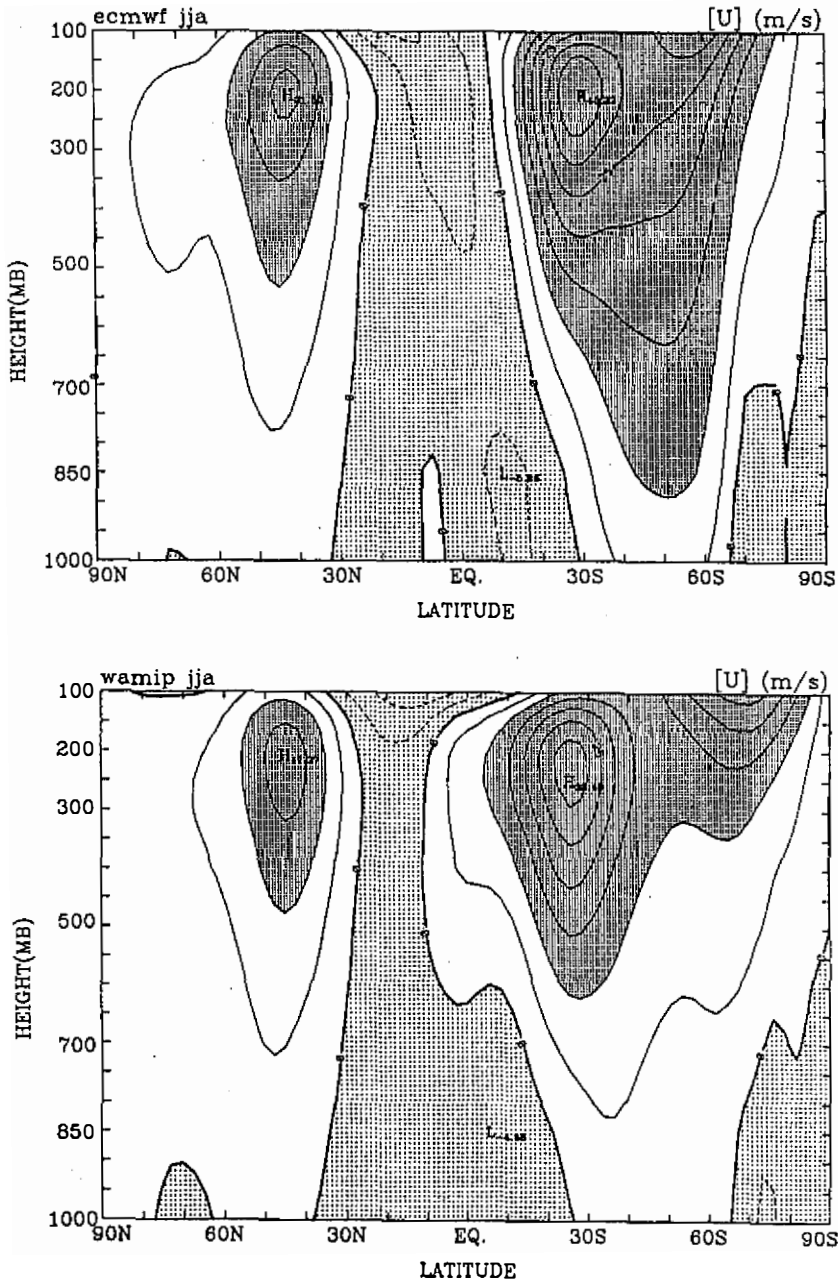


Fig. 2. Latitude-pressure distributions of zonal mean zonal wind (m/s) for JJA season according to (a) ECMWF analysis and (b) NTUGCM model simulation. Contour spacing: 5 m/s. Dark and light stippling indicate areas with  $U > 10$  and  $U < 0$  m/s, respectively.

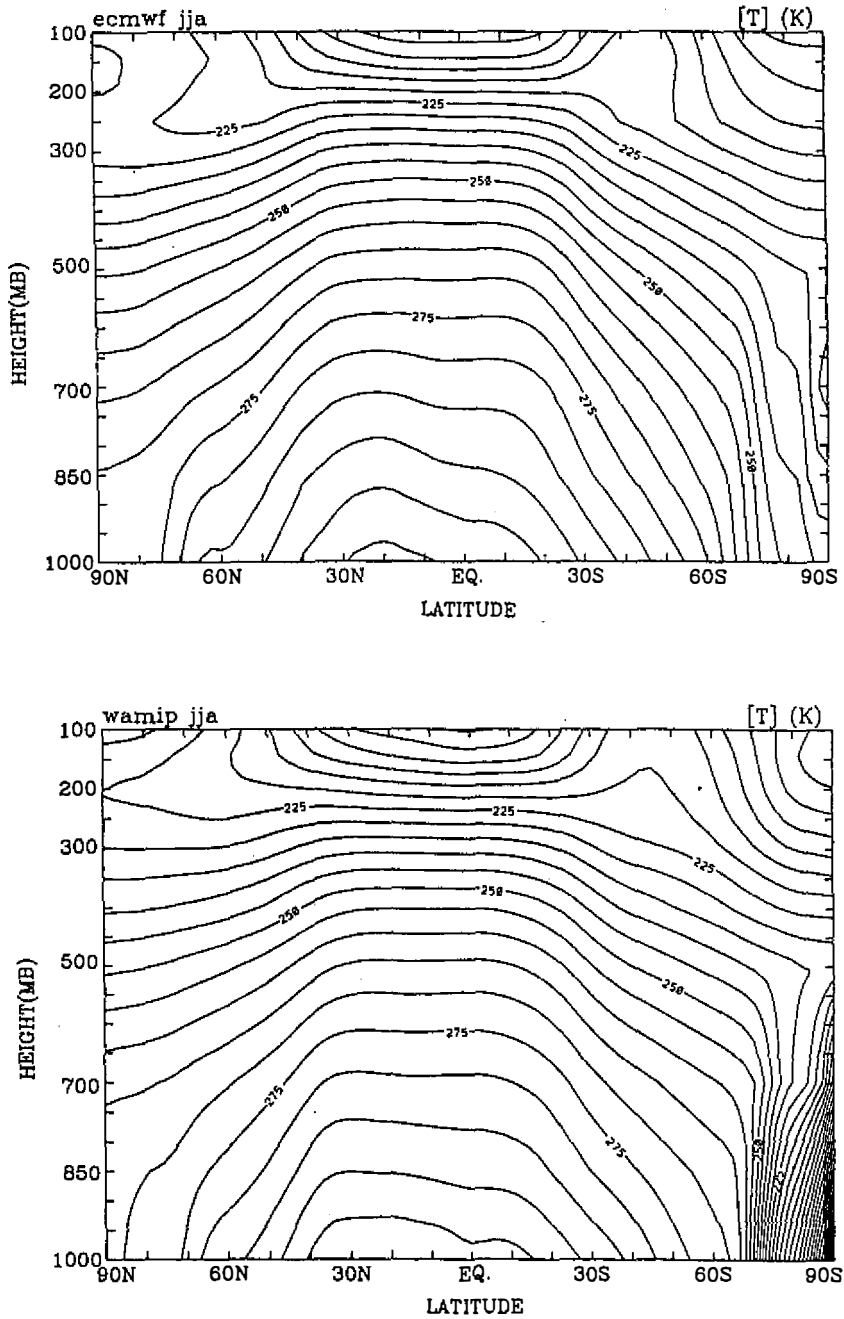


Fig. 3. Latitude-pressure distributions of zonal mean temperature (K) for JJA season according to (a) ECMWF analysis and (b) NTUGCM model simulation. Contour spacing: 5 K.

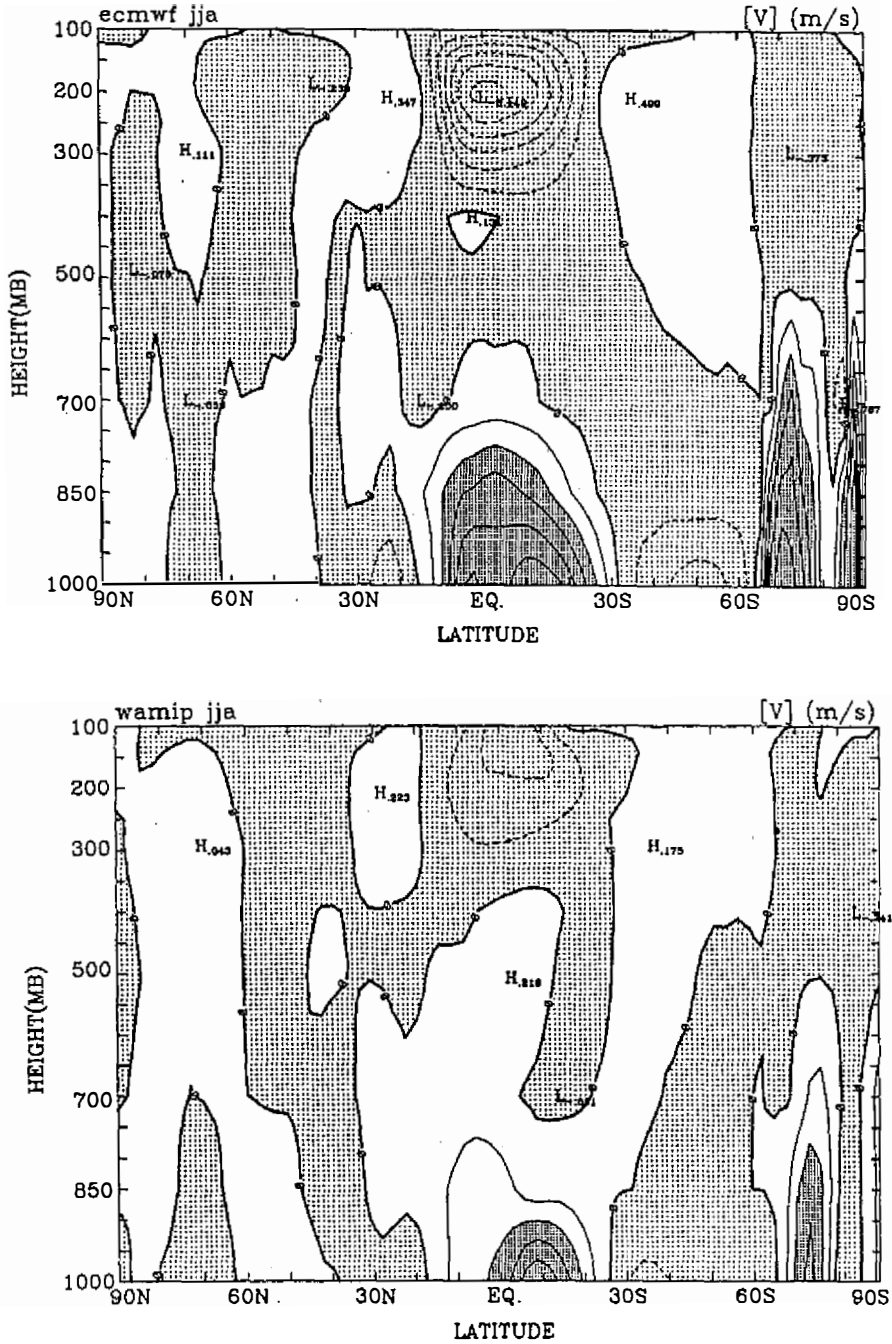


Fig. 4. Latitude-pressure distributions of zonal mean meridional wind (m/s) for JJA season according to (a) ECMWF analysis and (b) NTUGCM model simulation. Contour spacing:0.5 m/s. Dark and light stippling indicate areas with  $V > 0.5$  and  $V < 0$  m/s, respectively.

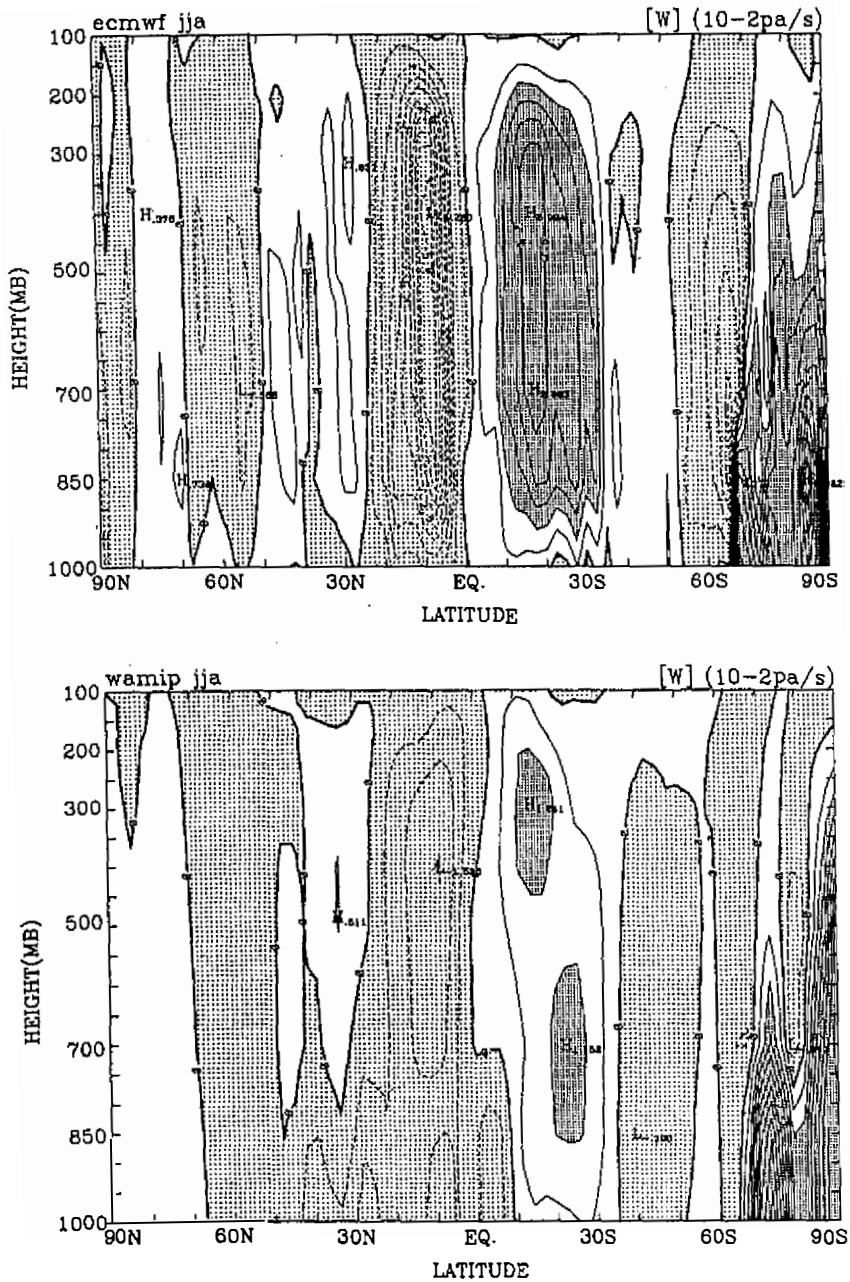


Fig. 5. Latitude-pressure distributions of zonal mean vertical velocity ( $10^{-2}$  Pa/s) for JJA season according to (a) ECMWF analysis and (b) NTUGCM model simulation. Contour spacing:  $0.5 \times 10^{-2}$  Pa/s. Dark and light stippling indicates areas with  $W > 0.5 \times 10^{-2}$  and  $W < 0$  Pa/s, respectively.

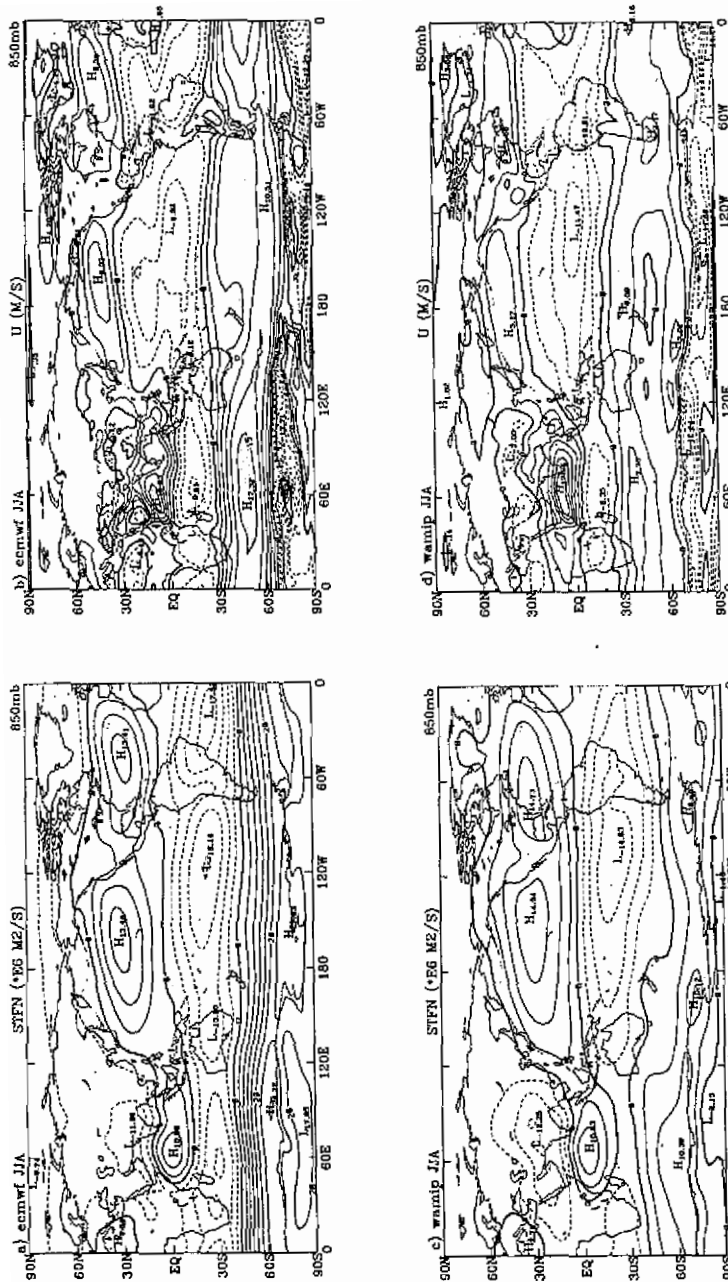


Fig. 6. Climatological distribution of (a) streamfunction( $10^6 \text{ m}^2/\text{s}$ ) and (b)zonal wind (m/s) at 850 hPa for JJA season based on ECMWF analysis, and (c) streamfunction, (d) zonal wind at 850 hPa by NTUGCM model simulation. Contour spacing for (a)&(c) are  $4 \times 10^6 \text{ m}^2/\text{s}$ , and for (b)&(d) are 3 m/s.

are weaker than the observed, but their counterparts in the Southern Hemisphere are stronger. The meridional gradient in the northern Indian Ocean is too strong, indicating that the simulated Somali jet is too strong (Figure 6). The simulated cyclonic circulation in South Asia covers the region from northern Africa to  $100^{\circ}$  E which is about the same size as observed. Figure 7 shows the stream function and zonal wind at 200hPa. The Tibetan high at 200hPa is well simulated. The Mexican high is missing and is replaced by a cyclonic circulation in the model climatology, which is accompanied by equatorial westerly flow from the dateline eastward to the Greenwich line as shown in Figure 7. In reality, the upper troposphere in the equator should be occupied by easterly flow as one can see in Figure 7a. This deficiency can also be seen in the zonal average (Figure 2). On the whole, the NTUGCM gives a better simulation at 850hPa than at 200hPa, and a better simulation around a large forcing region, *e.g.* South Asia, than around a weak forcing region, *e.g.* Eastern Pacific and South America.

The velocity of potential fields at 850hPa and 200hPa are shown in Figure 8. The tropical divergence field is as a whole weaker than the observed. In Asia and the Pacific, the centers of the observed velocity potential at both 850 hPa and 200hPa are located to the east of the Philippines. The model simulates both 850 hpa and 200 hpa velocity potential centers as being very close to the observation. The curvatures and the gradients of the observed velocity potential indicate two other convective regions, one in Northern Africa and the other in the Eastern Pacific and Southern America. However, the simulated results exhibit weaker convective activities in those two regions. The above deficiencies can be seen clearly in the precipitation field (Figure 9). There is generally good agreement between the observed and simulated precipitation patterns. The best simulation is found in the Asian monsoon region where the maximum precipitation occurs. However, the model precipitation is less than the observed precipitation both in the tropics and in the extra-tropics (outside the Asian monsoon area). This deficiency is consistent with the zonal means' biases discussed in the previous section.

#### 4. EAST ASIAN SUMMER MONSOON

The ASM constitutes a major circulation feature in the Northern Hemisphere. Tao and Chen (1987) have suggested that the EASM should be studied as a separate system because it behaves quite differently from the ISM. In fact, the EASM possesses a wide range of spatial and temporal scales of variability including the seasonal cycle, intra-seasonal oscillations, sub-seasonal scale, inter-monsoon interactions, sub-synoptic scale variability and super-cluster organization in the Western Pacific (Lau, 1992). Therefore, the EASM is much more complex than the ISM. A detailed discussion of the EASM should involve a diverse range of spatial and temporal scales. However, in this section we have only presented some of the important features of the simulated EASM.

##### 4.1 Monthly Mean Precipitation

Climatically, the summer monsoon rainfalls in East Asia include the pre-summer heavy rainfall in Southern China, the Mei-Yu season in Taiwan, the Mei-Yu over the Yangtze and Huaihe River Valleys and the mid-summer heavy rainfall in Northern China. Figure 10 shows the simulated monthly variations for the precipitation from May to August. It can be seen that

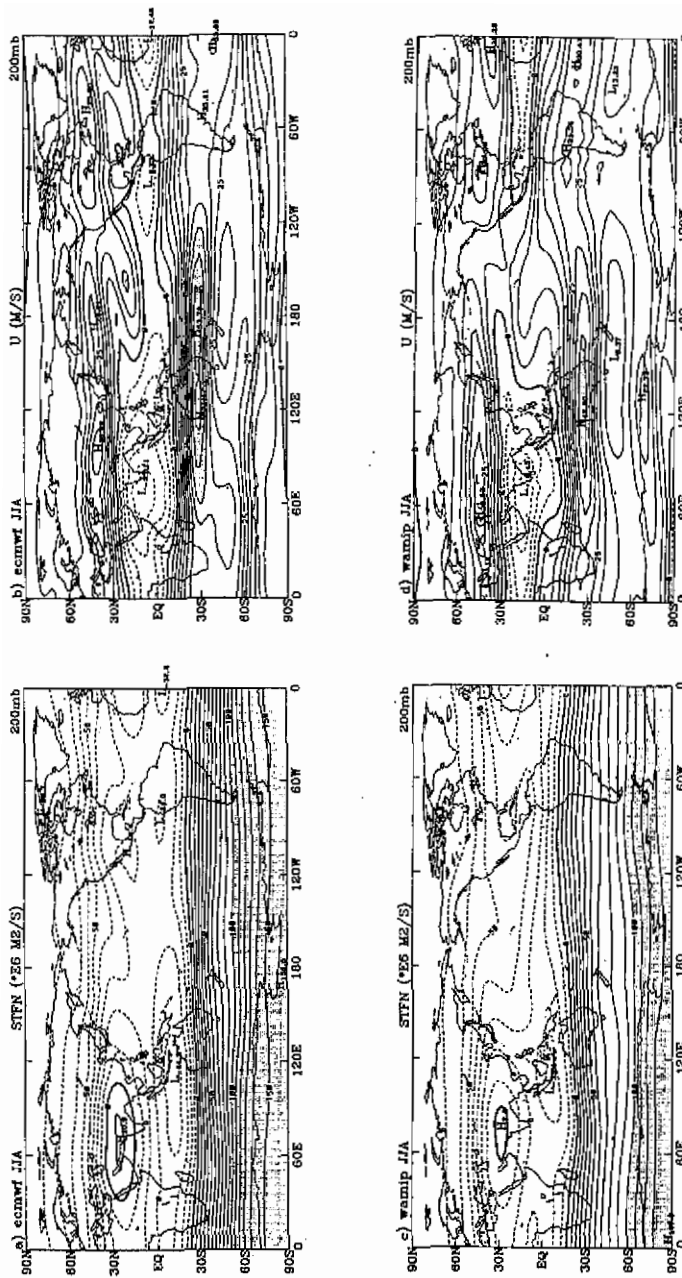


Fig. 7. Climatological distribution of (a) streamfunction( $10^6 \text{ m}^2/\text{s}$ ) and (b) zonal wind ( $\text{m/s}$ ) at 200 hPa for JJA season based on ECMWF analysis, and (c) streamfunction , (d) zonal wind at 200 hpa by NTUGCM model simulation. Contour spacing for (a)&(c) are  $4 \cdot 10^6 \text{ m}^2/\text{s}$ , and for (b)&(d) are  $5 \text{ m/s}$ .

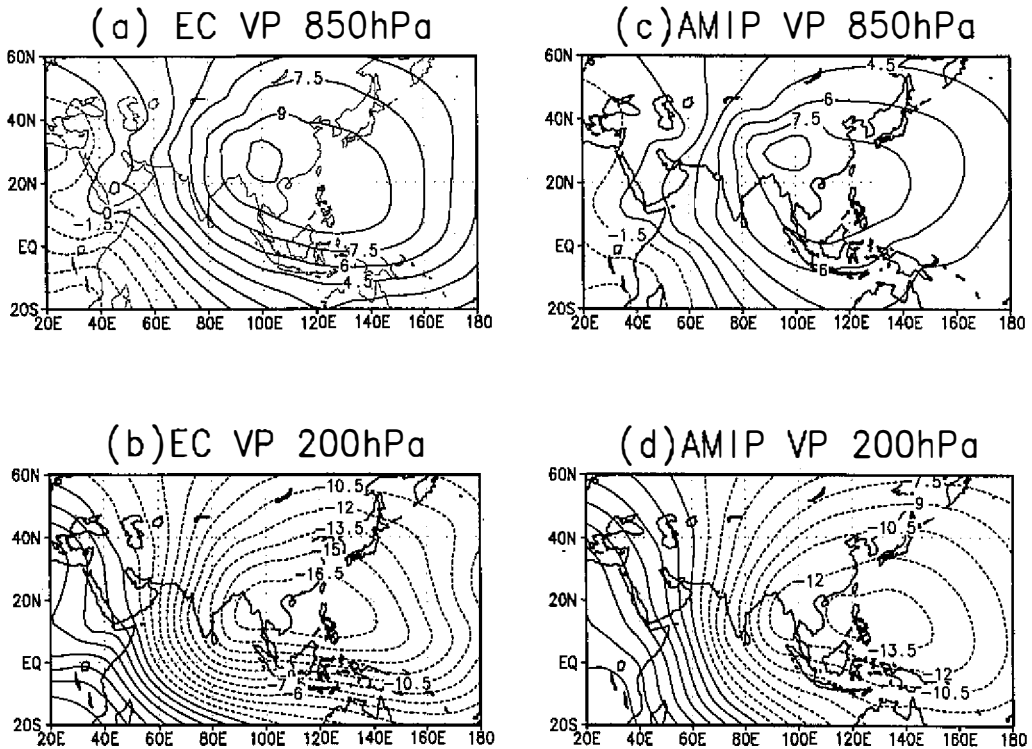


Fig. 8. Climatological distribution of velocity potential ( $10^6 \text{ m}^2/\text{s}$ ) for JJA season based on ECMWF analysis at (a) 850 hPa, (b) 200 hPa, and from NTUGCM model simulation at (c) 850 hPa, and (d) 200 hPa. Contour spacing:  $1.5 \times 10^6 \text{ m}^2/\text{s}$ .

the heaviest rainfall is mostly confined to the south and southeastern part of the Asian continent throughout the entire monsoon period except for July. In May, the heavy rainfall spreads over the Malay Peninsula, Borneo, Indo-China, the Bay of Bengal, Taiwan, Central China and Southern Japan. In June, the Mei-Yu rain band appears to be also connected with the heavy rain found over the East China Sea and Southern Japan. Other regions of abundant rain are found over the Indian Peninsula, the Bay of Bengal and Indochina. By July, the rain band appears to break up. One noticeable feature is that rainfall over Southern and Central China ( $25^\circ \text{N}$ ,  $110^\circ\text{--}120^\circ \text{E}$ ) decreases drastically. The heavy rainfall belt over China appears to split up into two with one over Northeastern China/Southern Japan and one over the southwestern part of China. In August, the basic rainfall pattern remains unchanged, although the amounts of rainfall appear to diminish considerably. The above features agree very well with the monthly mean rainfall climatology presented by Lau (1992). Figure 11 shows the latitude-time cross-sections of the 10-year mean annual cycle of Asian monsoon rainfall. The rainfall averages occurred between  $50^\circ \text{E}$  and  $120^\circ \text{E}$  for MSU and AMIP, respectively. This figure indicates a similarity in the phases of monsoon transitions between the observed and simulated rainfall. In

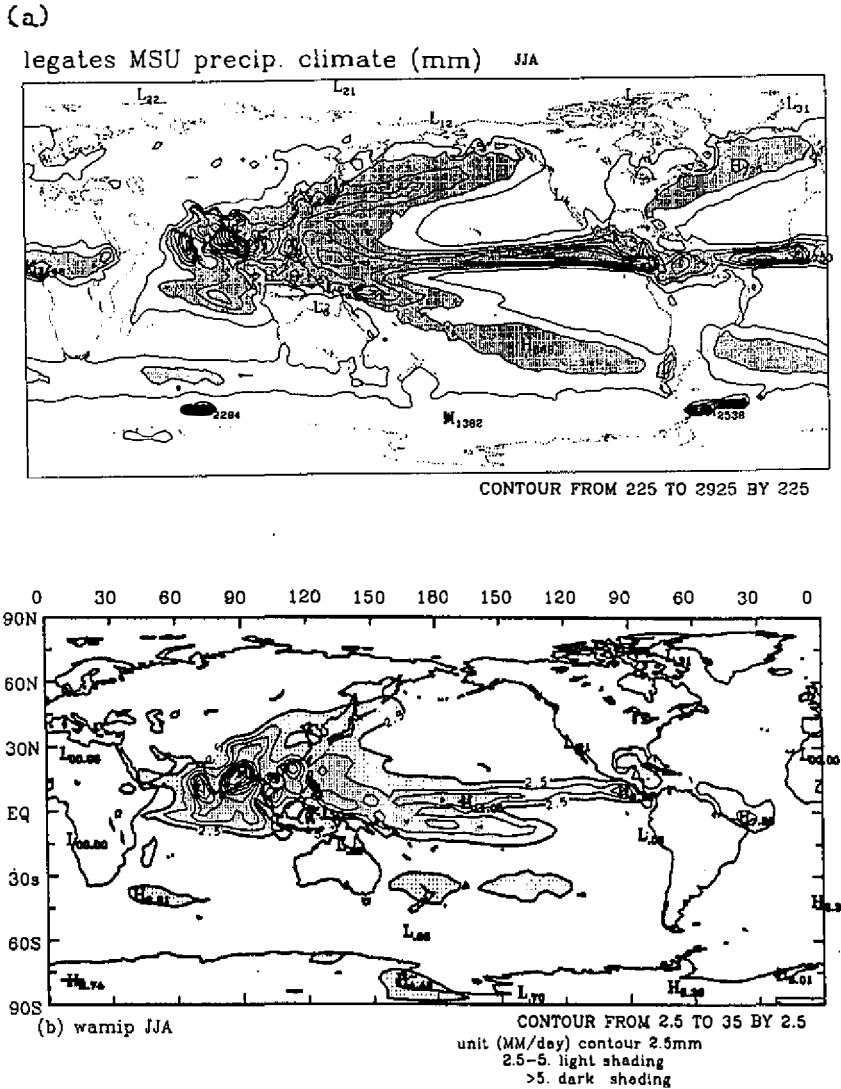


Fig. 9. Climatological distribution of precipitation(mm/day) for JJA season based on (a) Legates MSU data and (b) NTUGCM model simulation. Contour spacing: 2.5 mm/d. Shaded regions are precipitation > 2.5 mm/day.

both panels, monsoon rainfall attains a maximum magnitude in June and reaches its northernmost position during July-August. Similar to the observed, the model monsoon exhibits a sudden northward jump during a period from late boreal spring to early summer. The model produces a good precipitation rate during the summer monsoon period (slightly displaced to the south, however). While for the rest of the year the precipitation rate tends to be less than that observed.

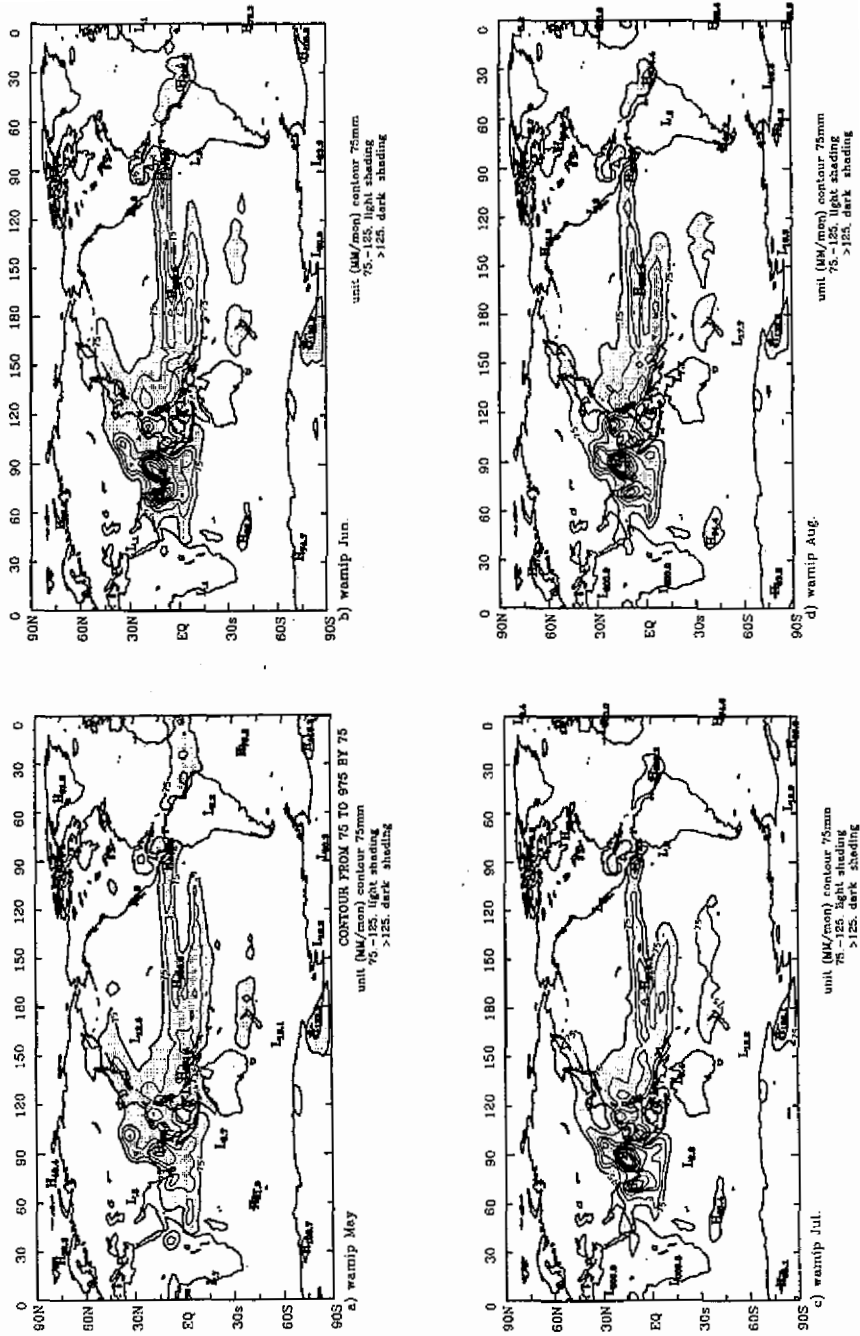


Fig. 10. Climatological distribution of precipitation(mm/month) for (a) May, (b) June, (c) July, and (d) August simulated by NTUGCM. Contour spacing: 75 mm/month. Shaded regions are precipitation > 75 mm/month.

## 4.2 Monthly Mean Large Scale Circulation

Figure 12 shows the climatological month-to-month variations of the flow pattern at 850hPa from May to August according to the ECWMF analysis. From this Figure we can see the following characteristics: (1) The development of the East Asian monsoon trough, (2) the eastward retreat of SH, (3) the development of the clockwise vorticity over the tropical Indian Ocean, and (4) the cross-equatorial southerly flow greatly intensifying over 30- 60°E and 100-120°E. In May the SCS and Southern China are dominated by a southwesterly flow coming from the Southern Asian monsoon region. Note that one branch of the southwesterly flow has its origin in Northern Australia and then crosses the equator in the Eastern Indian Ocean and southern part of the Bay of Bengal. In June, the southwesterly monsoon flow prevails over most of China and Japan, corresponding to the rainy season over the Yangtze River Valley and Japan. In July, the monsoon flow has a more southerly component and may reach deep into Northern China and even Northeastern China. From August, the summer monsoon flow begins to weaken. Figure 13 shows the simulated monthly variations of the flow pattern at 850 hpa as in Figure 12. In general the wind systems are well simulated. In particular, this model is able to capture the strength and position of the climatological trade winds and the southwesterly flow with remarkable skill over the Western Pacific and Asian areas. However, where southwesterly flow originates in Northern Australia these are not clear.

Figure 14 shows the climatological monthly mean wind vector at 200hPa from May to August from the ECWMF analysis. It can be seen that (1) the climatological upper anticyclone makes a northward motion shift to the Western Pacific to Burma-Thailand in May and moves towards the Tibetan Plateau in summer, (2) as the anticyclone center migrates northwestward, the 200hPa westerly flow in its northern flank retreats northward and weakens, while (3) the easterly flow to the south expands and strengthens and (4) the Pacific subtropical trough over the region south of 30°N gradually builds up and strengthens. The upper anticyclone has its largest amplitude in August. Diffluent upper level flows are a characteristic feature above the regions of monsoon rainfall. We also notice a pronounced cross-equatorial upper-level return flow, coming from the Western Pacific, across the SCS. Therefore, the low-level summer monsoon flow is accompanied by a process of inter-hemispheric mass exchange (Krishnamurti, 1985). Figure 15 shows the monthly mean wind vector at 200 hPa simulated by the NTUGCM. It can be seen that the model produces quite realistic wind field patterns over the Western Pacific and South Asia. These include the movement of the South Asia anticyclone, the weakening and northward retreats of the westerly flow, the expansion and strengthening of the easterly flow between 60 and 120° E, and the development of the Pacific subtropical trough over the Central Pacific around the dateline. However, the anti-clockwise circulation in the equator of the southern hemisphere around the dateline is completely missed by the model.

The tropical easterly jet stream (TEJ) in the upper troposphere is one of the important components of ASM systems and is also the major circulation feature in the tropical upper troposphere in the northern summer. TEJ establishment and activity are closely associated with the seasonal changes in the upper troposphere in the Northern Hemisphere, as well as the summer monsoon and precipitation events in South Asia and Southeast Asia. Based on the wind patterns at 200hPa, Ding *et al.* (1987) pointed out that the strongest easterly flow of the

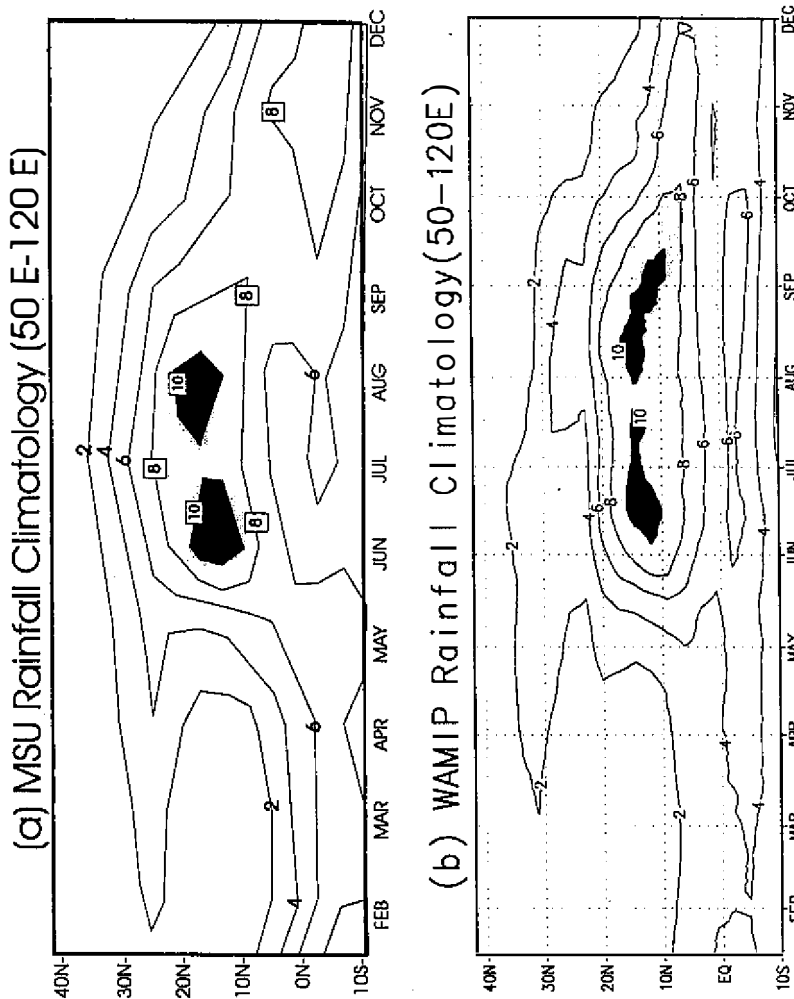


Fig. 11. Latitude-time sections of monthly precipitation (mm/d) climatology averaged over 50°E–120°E for (a) MSU and (b) NTUGCM model simulation. Contour spacing: 2 mm/d. Shaded regions are precipitation > 10 mm/d.

TEJ in May is located over the southern tip of the Indochina Peninsula. At this time the wind speed over India is weak. In June, the TEJ rapidly intensifies. The strongest easterly wind may be observed over the southern tip of the Indian Peninsula. During the same period the easterly jet markedly extends northward and a branch of easterlies occurs from 20 to 25° N over the western Pacific emerge with one branch which is located at the lower latitude. The above two branches of the easterly jet merge over Indo-China. In July, the easterly jet over South Asia significantly intensifies, and it also extends southward down to about 10° S. August is a month when the easterly jet reaches its maximum intensity. The evolution of the simulated monthly mean upper-level easterly jet in general is in good agreement with the above-mentioned fea-

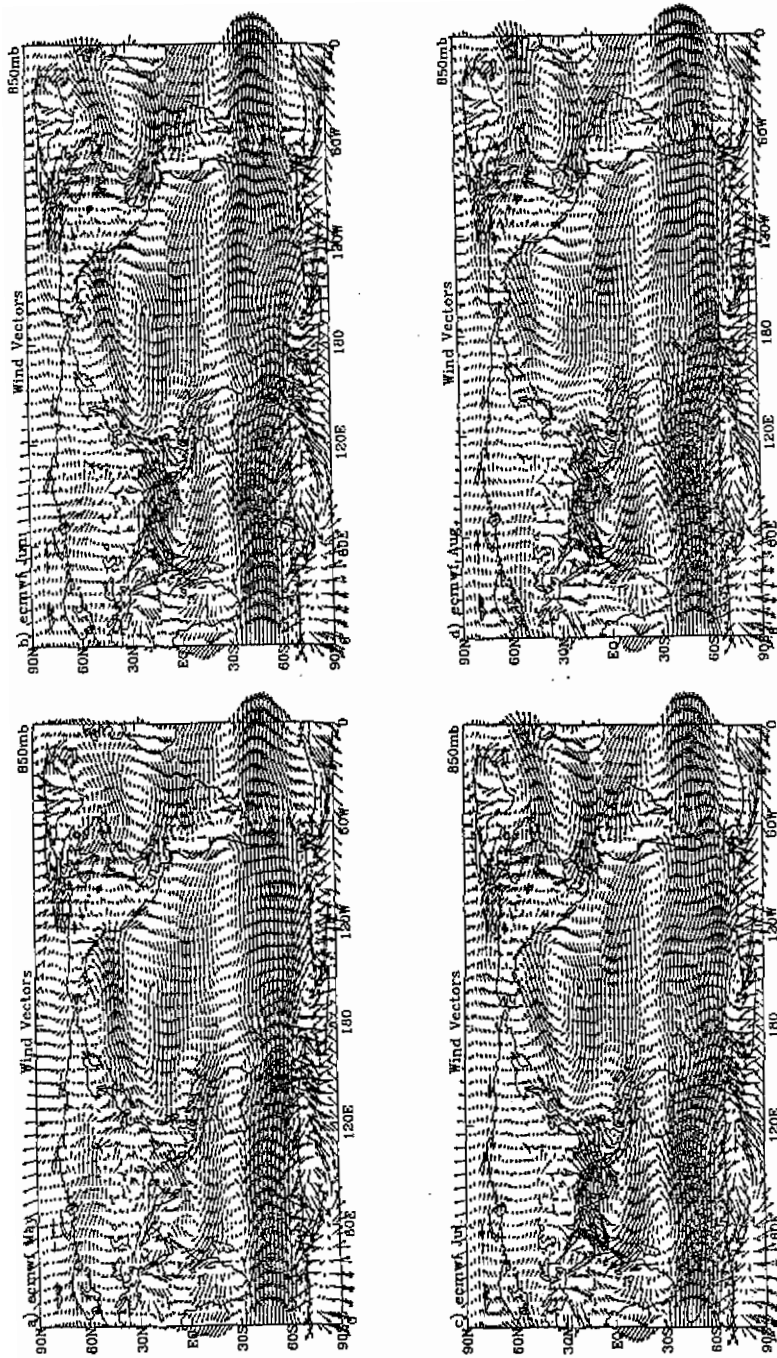


Fig. 12. Climatological distribution of wind vector at 850 hPa for (a) May, (b) June, (c) July, and (d) August based on ECMWF analysis. Stippling indicates areas with  $V > 15$  m/s .

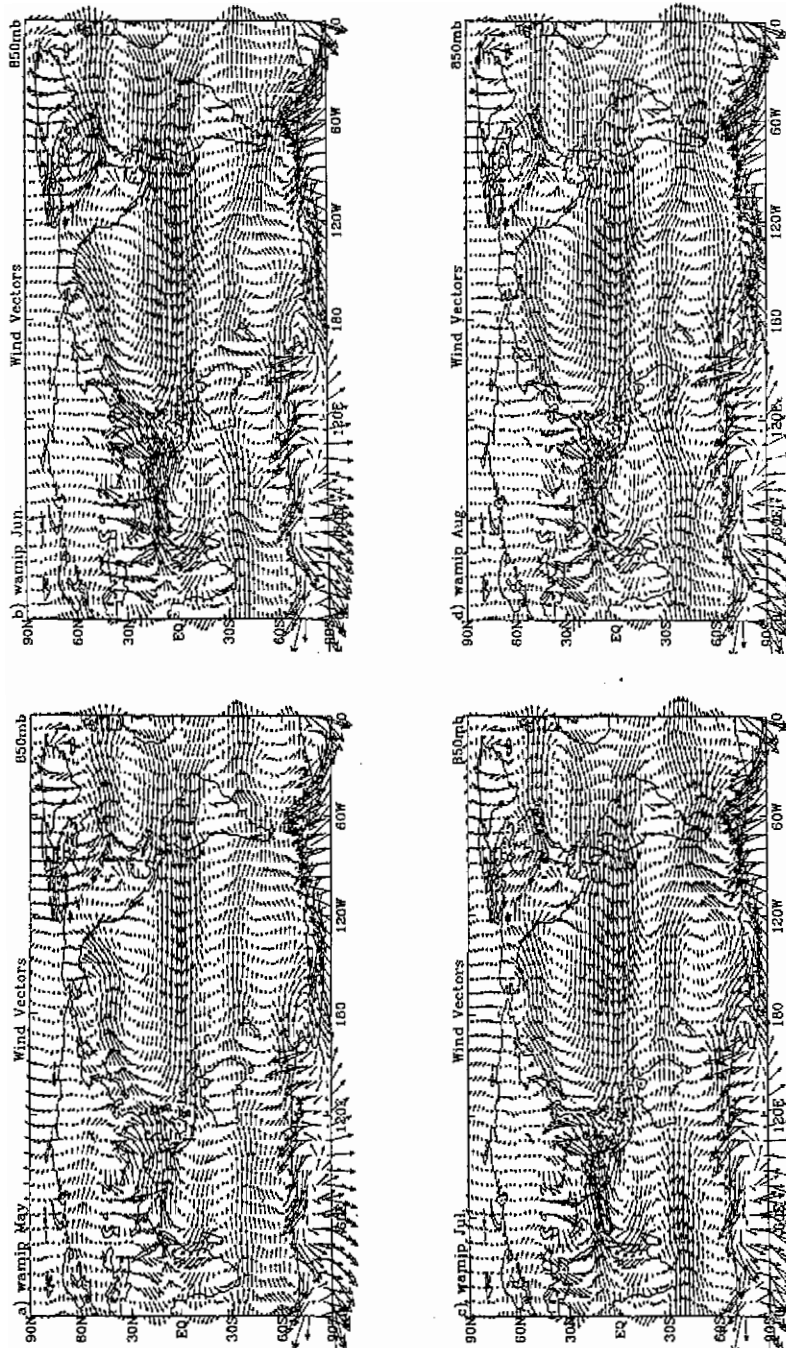


Fig. 13. Climatological distribution of wind vector at 850 hPa for (a) May, (b) June, (c) July, and (d) August simulated by NTUGCM. Stippling indicates areas with  $V > 15$  m/s .

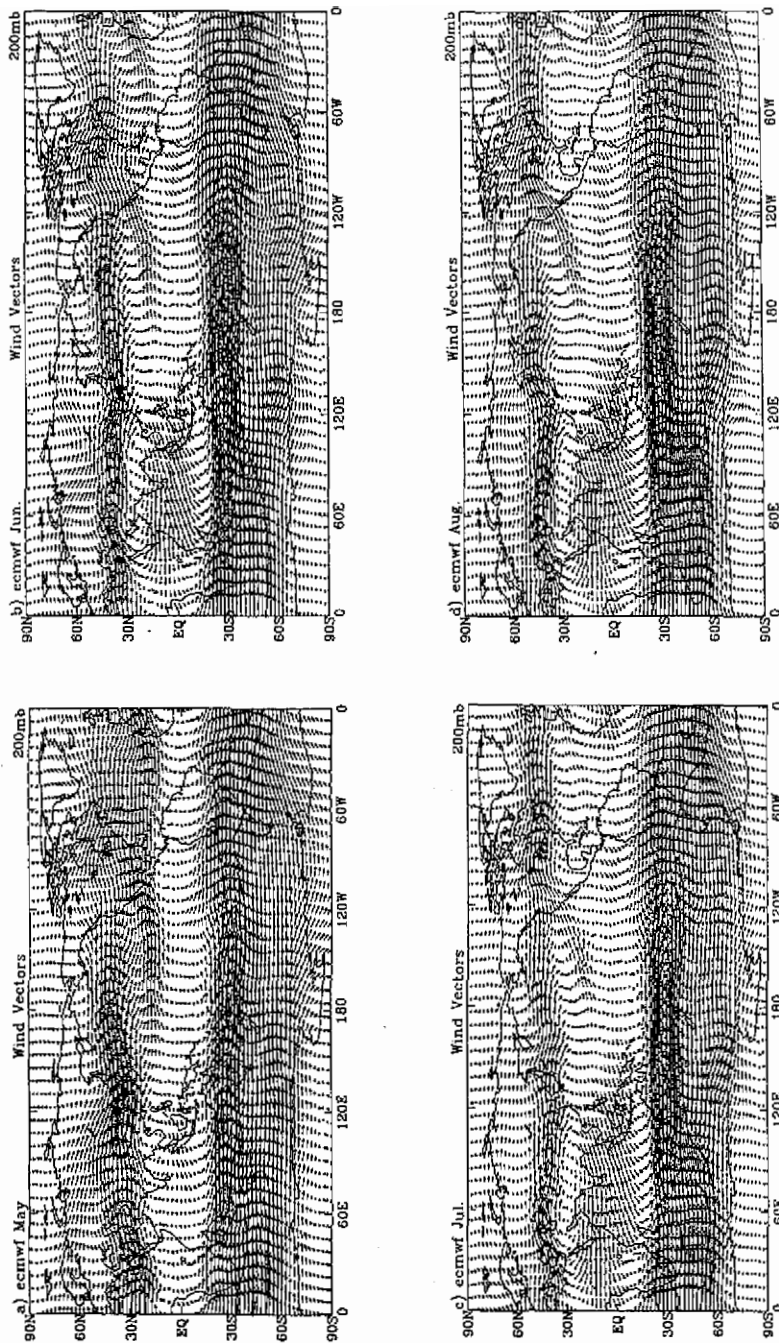


Fig. 14. Climatological distribution of wind vector at 200 hPa for (a) May, (b) June, (c) July, and (d) August based on ECMWF analysis. Stippling indicates areas with  $V > 30$  m/s .

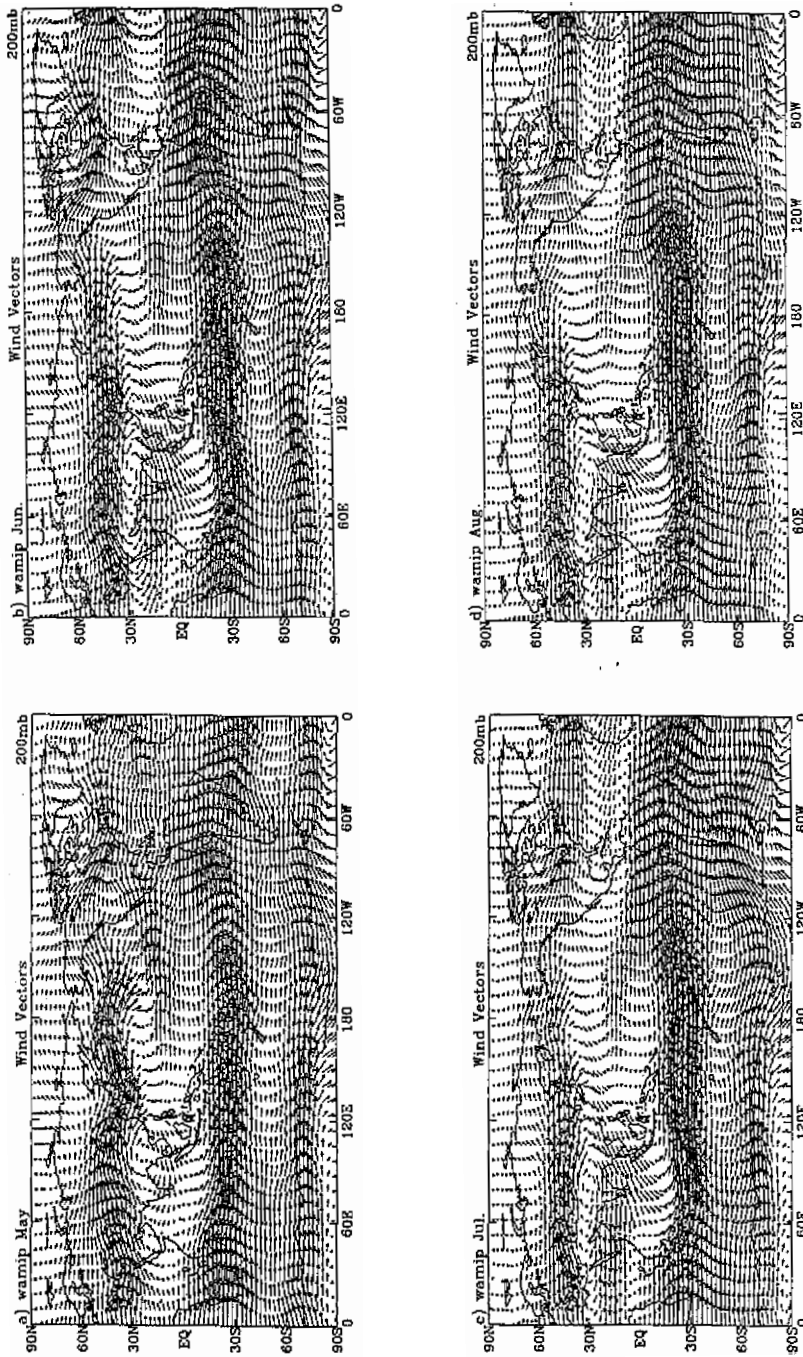


Fig. 15. Climatological distribution of wind vector at 200 hPa for (a) May, (b) June, (c) July, and (d) August simulated by NTUGCM. Stippling indicates areas with  $V > 30$  m/s .

tures. For example, in July, the TEJ has two branches. One is located around 20 to 25° N, extending from the northeastern part of the SCS westward to the Bay of Bengal and Southern India. The other is located around 5 to 10° N (barely seen), however, over the southern part of SCS. These two branches merge over the Arabian Sea.

### 4.3 Intraseasonal Variation

#### 4.3.1 Precipitation

Based on the latitude-time cross-section of the 10-day rainfall level in Eastern China (100-115°E) for 1961-1970 (Lau *et al.*, 1988) (Figure 16), we can see that the summer monsoon rainfall starts in the early part of May in Southern China (<30° N). At this time, Northern China and the Yangtze River Valley are dry. The rain band is basically stationary in the region to the south of the Nanling Mountains, which corresponds to the rainy season of Southern China (pre-summer rainy season) and the Mei-Yu season over Taiwan. This first standing stage of the major rain band generally continues until mid-June when it rapidly shifts to the Yangtze River Valley. The second standing stage starts the rainy season there (Mei-Yu). On average, the Mei-Yu season lasts for one month. From mid-July, the rain band moves over Northern China and in August further over Northeastern China, which is the northernmost position of the summer monsoon rainfalls. The third standing stage of the rain band causes a rainy season in the Northern part of China that generally lasts for one month. In the last part of August the rainy season of Northern China ends, with the major rain band retreating southward. At the end of August, it crosses the Yellow River and early in September, it moves back to Southern China. Note that from mid-July, the second rainy season predominates over Southern China, with a gap of one month between the pre-summer rainy season and this rainy season which is primarily caused by typhoons, ITCZ and other tropical disturbances. The simulated climatological mean of the time-latitude cross-section of the 10-day mean rainfall over Eastern China is shown in Figure 17. There is generally good agreement between the observed and simulated patterns. The first two standing stages and the second rainy season predominate over Southern China and are all well simulated. However, the third standing stage over Northern China is not well simulated.

The comparison of the NTUGCM with other AMIP models on the simulation of the EASM and the JJA precipitation has been plotted. Figure 18 (Wang *et al.*, 1997) shows the mean 1980-88 JJA precipitation for three regions averaged over 105-122° E in East China-the Northeast (35-45° N), Yangtze River Valley (25-35° N), and Southeast China (20-25° N), which are from observations (Tao *et al.*, 1991) and AMIP models. In Southeast China, where the level of rainfall is great (around 9.5 mm/d), values from two models (GFDL and NMC) are in good agreement with observations while the NTUGCM slightly under-estimates giving values of 7.9 mm/d. For the Yangtze River Valley and Northeast China, NTUGCM's values correspond statistically with observations, but a majority of the models over-estimate the precipitation.

### 4.3.2 Zonal wind

Figure 19 shows the time-latitude cross-section of zonal wind at 200hPa along 125° E between 10 to 50° N. Before mid-May, the upper level westerly jet is located at 37.5° N and the center of the easterly jet is at 15° N. The northward shift of the upper level jet occurs rapidly in 5 to 10 days at the beginning of June after which the westerly core is located over a stationary position near 40° N. At the same time, the center of the easterly jet moves northward to 20° N. At the end of July, a second northward transition occurs with the westerly jet shifting further in a similar manner to 45° N giving rise to the monsoon onset over North and North-eastern China (Lau *et al.*, 1988). The seasonal variations of the upper-level westerly and easterly jets is believed to be related to the movement of the South Asian upper-level anticyclone. The abruptness of the transition and the large extent of the area affected by the monsoon rainfall are unique features of the EASM rainfall that do not have a counterpart in the Indian region(Lau,1992).

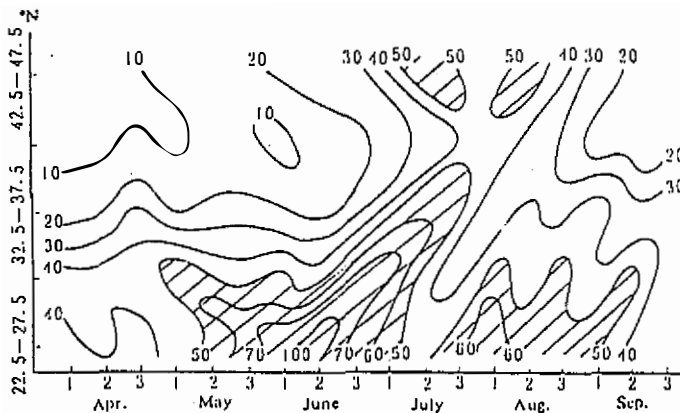


Fig. 16. Latitude-time section of 10-day mean precipitation (mm/10 day) amount in eastern part of China (100°E-115°E) for 1961-1970 during April to September(Lau, 1992). Contour spacing: 10 mm/(10 day). Shaded regions are precipitation > 50 mm/(10 day).

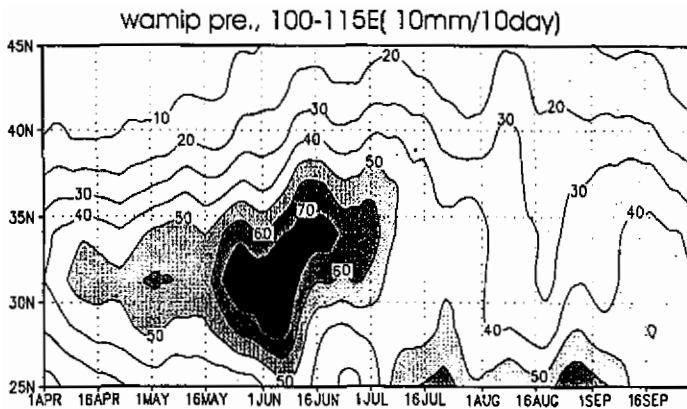


Fig. 17. Simulated latitude-time section of the 10-day mean precipitation (mm/10 day) amount in eastern part of China (100°E-115°E) during April to August. Contour spacing: 1 mm/d. Shaded regions represent precipitation > 50 mm/(10 day).

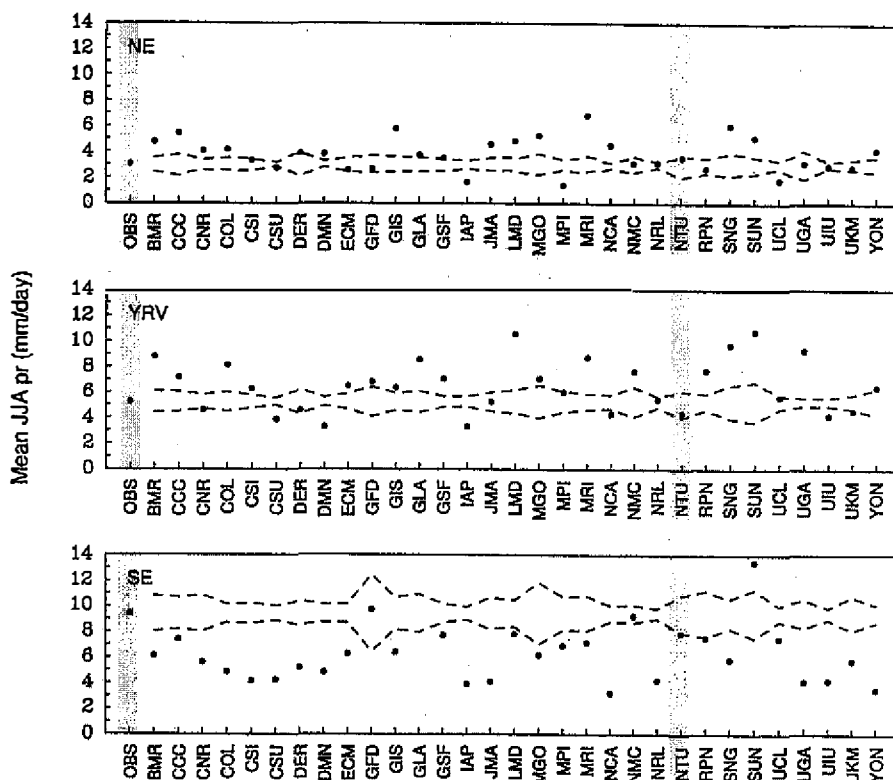


Fig. 18. Mean 1980-88 summer (JJA) precipitation (mm/d) for observation (OBS) and AMIP GCMs over three regions averaged over  $105-122^{\circ}\text{E}$  (NE:  $35-45^{\circ}\text{E}$ , yrv:  $25-35^{\circ}\text{N}$  and SE:  $20-25^{\circ}\text{N}$ ). Dashed line represent t-test 99% confidence interval that GCM means are same as observation (Wang *et al.*, 1997)

### 4.3.3 Sub-tropical height over the western Pacific Ocean

SH is one important component of the EASM system. The SH over the Western Pacific assumes a marked seasonal variation in respect to its position. As the summer monsoon develops from spring to summer, the SH continuously moves northward. The seasonal shift in the position of the SH shows up as an alternation of gradual shifts and abrupt jumps, which are closely related to the advance and retreat of major rain bands in Eastern China. In general, three abrupt northward jumps may be observed (Ding, 1994). The first northward jump occurs in the middle or last part of June, with the ridge line of the high moving over to  $20-25^{\circ}\text{N}$ . This indicates a northward jump of the rain-belt over the Yangtze and Huaihe River Valleys, heralding the end of both the pre-summer season over south China and the Mei-Yu season over Taiwan. The second northward jump of the SH occurs in the early and middle part of July. The ridge line of the high reaches to  $25-30^{\circ}\text{N}$ , starting the rainy season in the Yellow River and

Huaihe River Valleys and ending in the rainy season in the Yangtze River Valley. The third northward jump occurs in the last part of July and early in August. This jump brings the ridge line of the SH over the region around  $30^{\circ}$  N, thus leading to the beginning of the rainy season in Northern China and the dry season in the Yangtze River Valley. Figure 20 shows the simulated 850hPa ridge line of the SH at the longitudinal range of  $130-140^{\circ}$  E from 20 May till the end of August. It can be seen that the model produces three quite realistically northward jumps for the SH. These are: the first northward jump occurring on 6 to 11 June, when the ridge line moves from  $15^{\circ}$  N to  $21^{\circ}$  N; the second jump at around 26 June, where its ridge line moves northward to  $26^{\circ}$  N; the third northward jump occurring on 21 to 25 July with its ridge line moving to  $30^{\circ}$  N. These features agree very well with the above climatological analysis. The first simulated jump of the SH coincides with the northward propagation of the rain belt over the Yangtze River Valley, while the second simulated jump corresponds with the end of the rainy season in the Yangtze River Valley as shown in Figure 17.

#### 4.3.4 South Asian anticyclone

The seasonal migration of the high-level anticyclone is strongly related to the establishment of the process of the summer monsoons over Asia. He *et al.* (1987) analyzed the case of 1979, and identified two periods of drastic change in the anticyclones at 200hPa, which coincide with the two transition periods of the low-level flow and precipitation patterns, respectively. During the first transition the anticyclone center moves rapidly northward (11-15 May). The second transition (15-19 June) is characterized by the appearance of the western center over the Saudi Arabia-Iran region. Figure 21 shows the successive 5-day mean position of the anticyclone at 200hPa for the thirteen sub-periods (starting 1 May) simulated by the AMIP

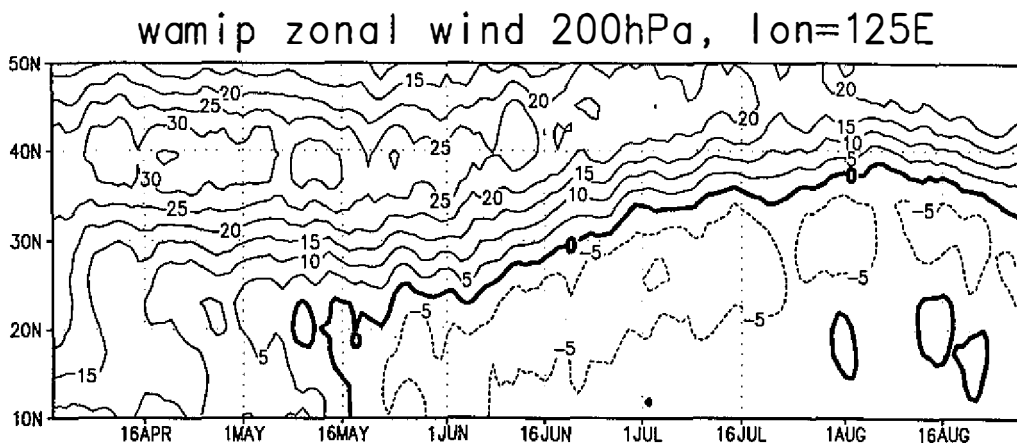


Fig. 19. Simulated climatological-mean of time-latitude section of zonal wind (m/s) at 200 hPa along  $125^{\circ}$  E between  $10^{\circ}$  N to  $50^{\circ}$  N. Contour spacing: 5 m/s.

integration. From the movement of the 200hPa anticyclone center we can find the center moves rapidly northeastward during the first three sub-periods. After sub-period 4 (16-20 May) the center shifts westward to  $90^{\circ}$  E near  $26^{\circ}$  N, where it then stays for the next four sub-periods (21 May to 10 June). The anticyclone center then moves northwestward after sub-period 8 (6-10 June). The appearance of the western center over the Saudi Arabia-Iran region occurs in sub-period 11(20-24 June).

#### 4.3.5 Cross-equatorial flow

The summer monsoon in South Asia is believed to be closely related to the cross-equatorial air flows. Findlater (1969) discovered the existence of the Somali low-level jet anchored off Eastern Africa. Tao *et al.* (1962) pointed out that when a meridional type of circulation prevailed over East Asia, the probability of a northward transport for the air of the Southern Hemisphere near the equator is very high. Some studies have revealed that, from the East African coast to the central Pacific, there are several cross-equatorial air flows, of them, the most obvious is the Somali Jet. This jet originates in the South Indian Ocean (around the Mascarene high), then flows northwestward with the southeast trade wind and runs into the southwest monsoonal flow in the Northern Hemisphere while crossing the equator. Further east, in the Eastern Indian Ocean ( $80-85^{\circ}$  E), there is likely to be another cross-equatorial airflow, while over the SCS and the Western Pacific, there are three possible cross-equatorial airflows that are located at  $105-110^{\circ}$  E,  $125-130^{\circ}$  E and  $140-150^{\circ}$  E respectively. The cross-equatorial flow at  $140-150^{\circ}$  E is very steady and the other two flows are more variable, with

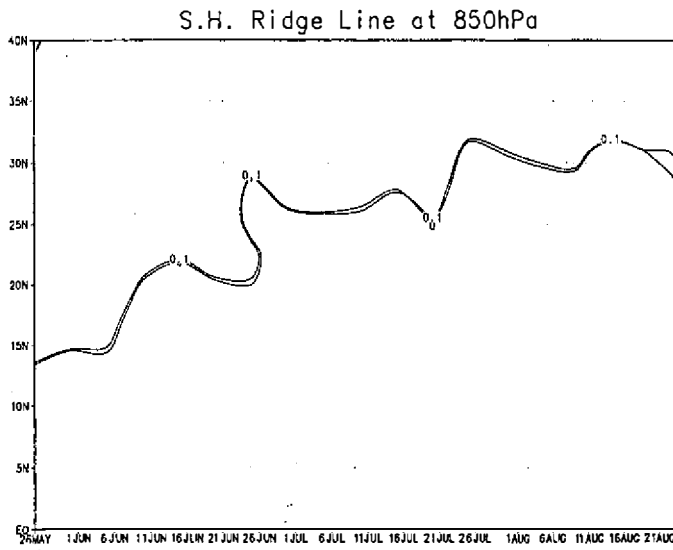


Fig. 20. Simulated climatological-mean of ridge line of subtropical high at 850 hPa between  $130^{\circ}$  E- $140^{\circ}$  E from 20 May till August( 5-day running mean).

the flow at 105-110° E being stronger than the other two. Wang and Li (1982) indicated that the beginning and maintenance of the Mei-Yu is also related to the cross-equatorial flow at about 110° E. Figure 22 shows the climatological mean of the time-longitude cross-section of the simulated cross-equatorial flow at 850 hPa in the equatorial region from 30 to 180° E. From this Figure, we can see two strips of stable and steady southerly flows. One is located around 40° E, which is the Somali Jet, and the other is between 140-150° E. These two stable southerly flows are in good agreement with the observation. There is another stable southerly flow that wanders between 110 and 120° E, where its intensity varies greatly with time. During the period of May, we can also find a southerly flow that extends eastward from 70° E to 100° E. At the same time there is another steady cross-equatorial flow located at 85-90° E.

#### 4.4 Onset of the EASM

The onset of the EASM (or the first transition of the ASM) has received much less attention than that of the ISM. Hsu and Chen (1997) (hereafter referred to as HC) have recently investigated the characteristics of large-scale circulation during the first transition of the ASM by a compositing technique based on the ECMWF analysis. In this section, we will closely follow their studies. Figure 23 plots a Hovmiller diagram for (a) the 500-200 hPa mean temperature averaged over 30-35° N, (b) the OLR (Outgoing Long wave Radiation) averaged over 10-15° N, (c) OLR averaged over 110-120° E, and (d) 850 hPa zonal wind averaged over 110-120° E by HC. These plots display the climatologically temporal variation of five-day running means from April to August. In Figure 23a a mean value, obtained by averaging the temperature over the region from April to August, is subtracted to show the warming more clearly. From this Figure we can see the temperature anomalies turn positive in mid-May, making the occurrence of the first transition. A later warming period in the region from 50 to 130° E, marks the second transition, which occurs in early June and persists through to the end of June. This process coincides with the seasonal variation of heating over the Tibetan Plateau and the resultant seasonal evolution of temperature and height fields. The maximum temperature anomalies, located near 90° E, persist from June to August. The thermal condition of the Tibetan Plateau may cause not only the variations in the circulation system over the plateau and its surrounding areas, but also the planetary scale circulation anomalies (Huang, 1985). Figure 23b indicates that the convection activities from 90 to 110° E start in early April. The convection between 75 and 80° E also starts in early April but is weaker than its counterpart between 110 and 120° E. The convection is restricted in these two regions and remains localized until mid-May when it occurs simultaneously over a much broader region. This later onset of the convection coincides with the first transition shown in Figure 23a. In early June, the convection simultaneously occurs over an even larger region, from the Arabian Sea to the Philippines and coincides with the second transition. As depicted in Figure 23b, mid-May and early June mark the first and second transitions of the ASM, respectively. The two features also exhibit distinct characteristics. From Figures 23c and 23d we can find a dramatic change occurs in 110-120° E when the 850 hPa zonal wind, averaged between the equator and 15° N, changes from easterly to westerly in mid-May. The westerly then persists throughout August. The OLR field also abruptly changes when the values in the SCS drop from 250  $\text{W/m}^2$  to less than

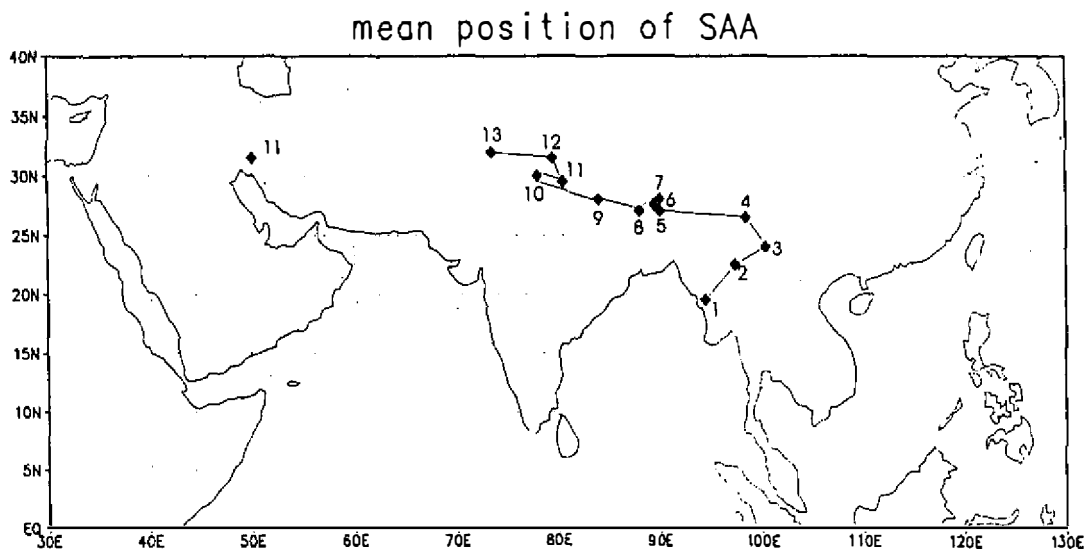


Fig. 21. Simulated climatological-mean of center of South Asian anticyclone at 200 hPa for 13 subperiods (5-day mean position starts at 1 May).

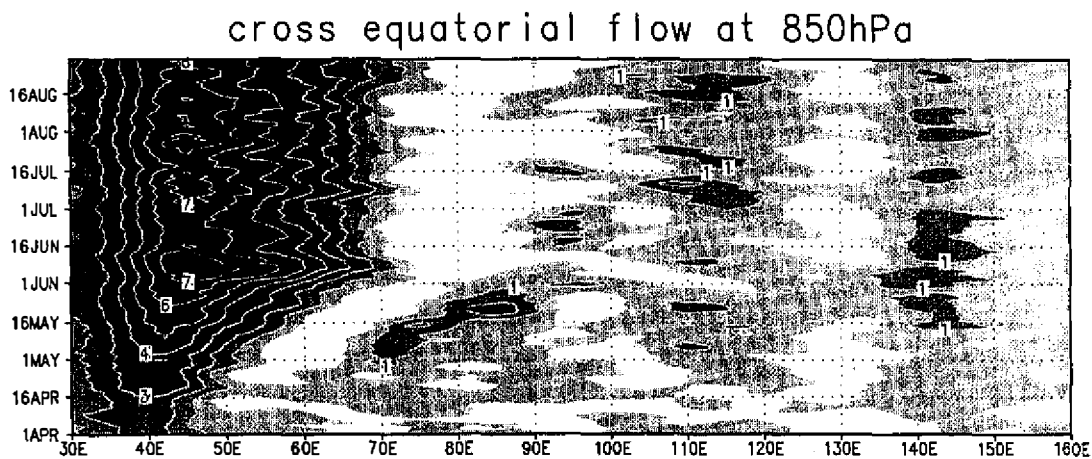
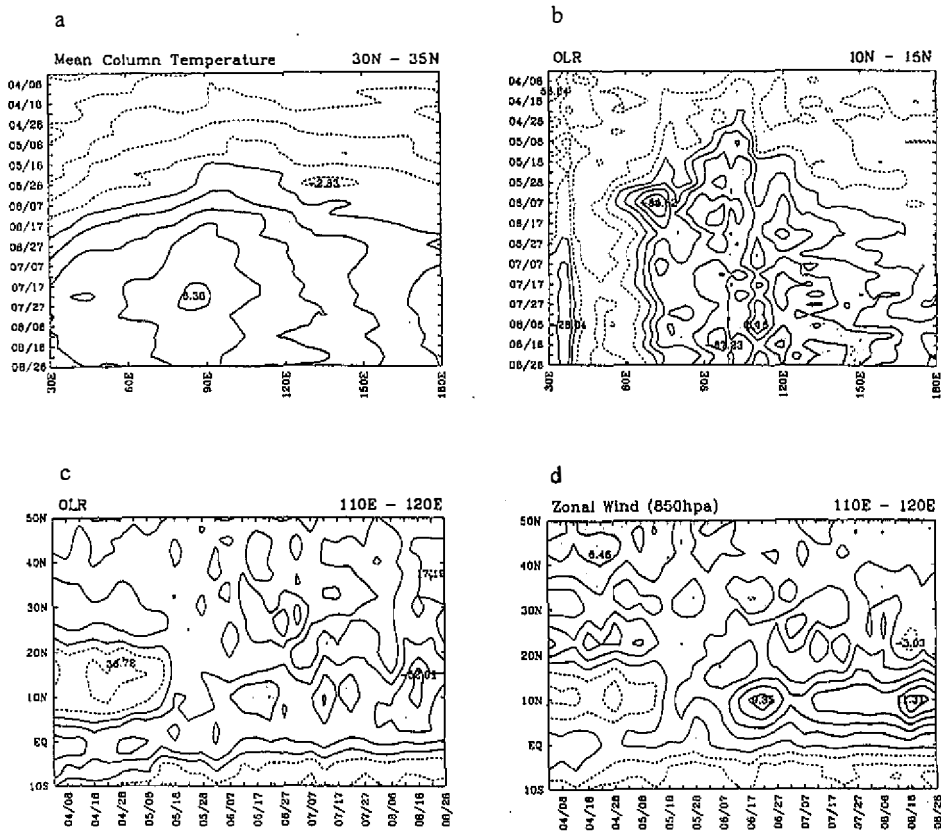


Fig. 22. Simulated climatological-mean of time-longitude section of cross-equatorial flow (m/s) at 850 hPa in equatorial region.

220  $w/m^2$  in mid-May. The second drop of the OLR occurs in early June, marking the second transition.

Figure 24 is the same as Figure 23 except that it is from the AMIP simulation, where the

OLR fields are replaced by the model's precipitation. Comparing Figures 24a and 23a, we can see that the model and observed temperature fields show fairly good agreement. The simulated temperature anomalies turn positive on 13 May, and the warming in the region from 30 to 150° E occurs on 9 June. Also, we can see the maximum temperature anomalies located near 90° E and these persist from June to August. From Figure 24b we can see that the large increase in convection around 110° E is on 12 May, and in early June, the convection simultaneously occurs over the three bay areas in South Asia. These two events agree very well with



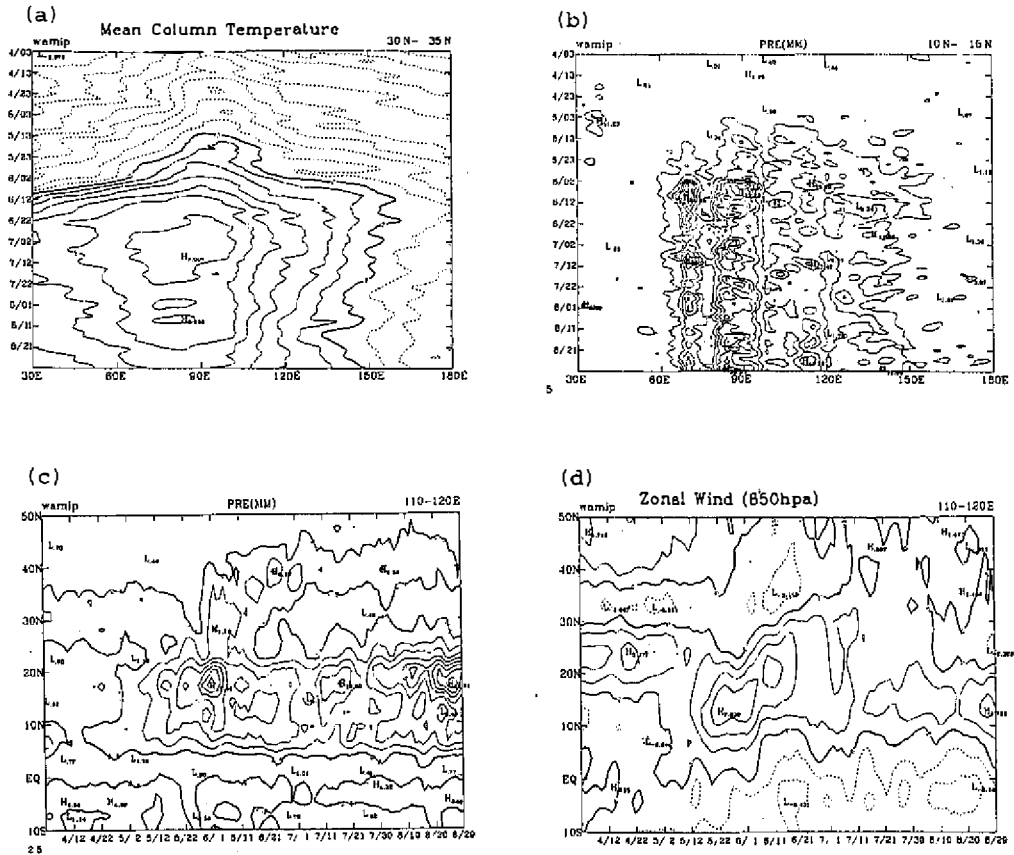
**Fig. 23.** Hovmill diagrams for 5-day running means of following variables: (a) 500-200 hPa mean temperature (K) averaged over 30°N- 35°N OLR( $W/m^2$ ) averaged over 10 °N-15 °N, (c) OLR( $W/m^2$ ) averaged over 110 °E-120 °E, and (d) 850 hPa zonal wind (m/s) averaged over 110 °E-120 °E. Value 246K and 240  $W/m^2$  have been subtracted from temperature and OLR, respectively. For temperature, contour interval 2K and values greater than zero are shaded. For OLR, contour interval 15  $W/m^2$  and values less than zero are shaded. For zonal wind, contour interval 2 m/s and values in excess of 2 m/s shaded.

Figure 23b. Figure 24c indicates that the simulated precipitation between 5 and 20° N suddenly increases from 2.5 mm/d to 5 mm/d on 10 May and then persists until September. The rain band propagates northward in late May and early June. From Figure 24d we can see that an abrupt switch of the 850hPa zonal wind from easterly to westerly, between the equator and 15° N, occurs in early May. The westerly then persists throughout August. Note that the westerly wind greatly intensifies in mid-May and gradually moves northward to mid-latitude. Comparing the model simulations of Figures 24c and 24d with observations, we can see the general agreement between them. However, the simulated onset day of the EASM seems earlier than the climatology, and the rainband is a few degrees north of that observed. In order to see the onset date of the EASM more clearly, Figure 25 plots the evolution of the SH ridge line at 850 hPa and five-day means from 28 April to 27 May are plotted. From this Figure we can see the SH retreats in an eastward direction over the SCS and the onset date of the EASM could be set around 13 to 17 May (i.e. sub-period 4). Figure 26 shows the time-latitude cross-section of southwesterly wind at 850hPa, averaged between 110 to 130° E. From this figure we can notice that the southwesterly wind greatly increases between 10° N and 25° N around 14 May. Based on the above discussion, we therefore conclude that the AMIP simulation of the NTUGCM for the onset date of the EASM is set at 13 May.

## 5. SUMMARY AND CONCLUSIONS

Based on the NMC spectral model with significant modifications of virtually all of the physical parameters, we have developed the NTUGCM. In this study the NTUGCM was used to perform an AMIP integration from 1 January 1979 to 31 December 1988. In general the model appears to simulate the global climate with a degree of skill similar to that of most comparable models (*e.g.* Boer *et al.* 1991). For the latitude-pressure distribution of zonal means of atmospheric variables for the seasons of JJA, the location and strength of the simulated jets in the extra-tropics of the Northern and Southern Hemispheres are quite similar to those observed. However, the model bias indicates that the troposphere is colder, that the tropical easterly flow is too small in the middle troposphere and that the Hadley and Ferrel cells are weaker than those observed. These biases are caused primarily by a lack of latent heat exchange between the ocean surface and the atmosphere, mostly in the equatorial Central and Eastern Pacific. Another contributing factor might be the excessive radiative cooling caused mainly by tropical cirrus cloud. For the global projection of the JJA climatology, the simulated stream function at 850 hPa captures most of the major features in the observed climatological-mean fields, i. e. the SH over the ocean, the cyclonic circulation over South Asia and the eddy straddling the equator in the Indian Ocean, as well as the Tibetan high, simulated in the 200 hPa stream function. In general, the NTUGCM gives a better simulation at 850 hPa than at 200 hPa and a better simulation around a large forcing region, *e.g.* South Asia, than around a weak forcing region, *e.g.* the Eastern Pacific and South American coast. The best simulation for precipitation is found in the Asian monsoon region where maximum precipitation occurs.

It is well known that the land-ocean heat contrast caused by the seasonal variations in solar radiation provide a basic framework for the large-scale monsoon circulation. If inter-annual variation in large scale monsoon circulation is determined presumably by lower boundary



**Fig. 24.** Simulated climatological-mean of Hovmill diagrams for 5-day running means of following variables: (a) 500-200 hPa mean temperature (K) averaged over 30°N-35°N, (b) precipitation (mm/d) averaged over 10°N-15°N, (c) precipitation (mm/d) averaged over 110°E-120°E, and (d) 850 hPa zonal wind (m/s) averaged over 110°E-120°E. Value 246K has been subtracted from temperature. For temperature, contour interval 2K and values greater than zero are shaded. For precipitation, contour interval 2.5 mm/d and values greater than zero are shaded. For zonal wind, contour interval 2 m/s and values in excess of 2 m/s are shaded.

forces, they could, in principle, be simulated reasonably well by the GCM, with integration of specified observed lower boundary conditions to suppress the nonlinearity of the internal atmospheric dynamics. Therefore, the prediction of the monsoon may be feasible, as long as the lower boundary forcing is large enough to act as a driving force for the monsoon circulation. Among monsoon regions, however, the most important are the South and the East Asian monsoon regions. East Asia is the region with which we are most concerned. The geography of

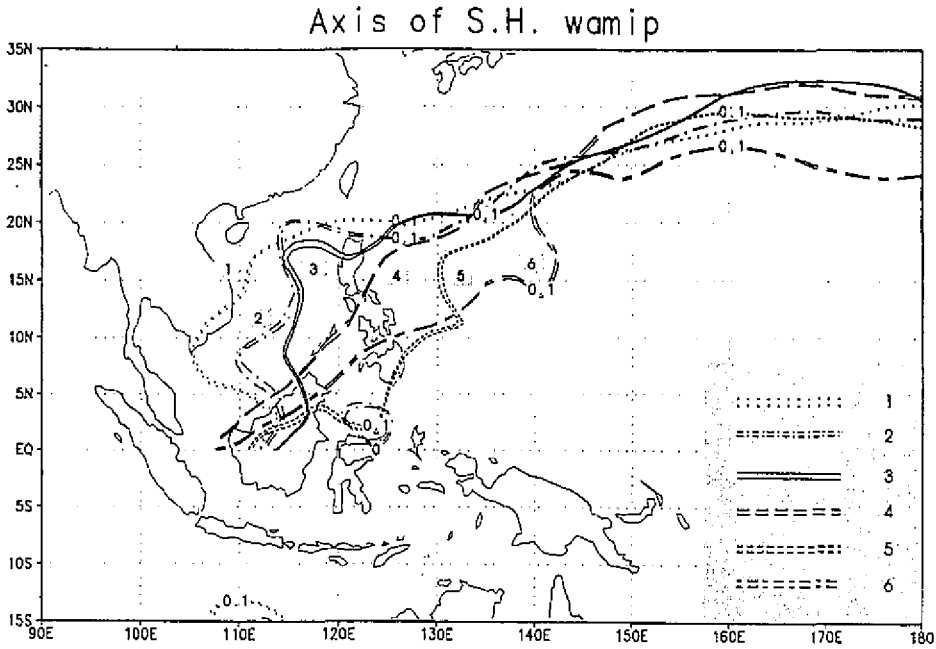


Fig. 25. Simulated climatological-mean of the evolution of the subtropical high's ridge line at 850 hPa for six 5-day mean from 28 April to 27 May. (The six subperiods are : 1 : 4/28-5/2 , 2: 5/3-5/7 , 3: 5/8-5/12 , 4:5/13-5/17 , 5:5/18-5/22 , 6:5/23-5/27)

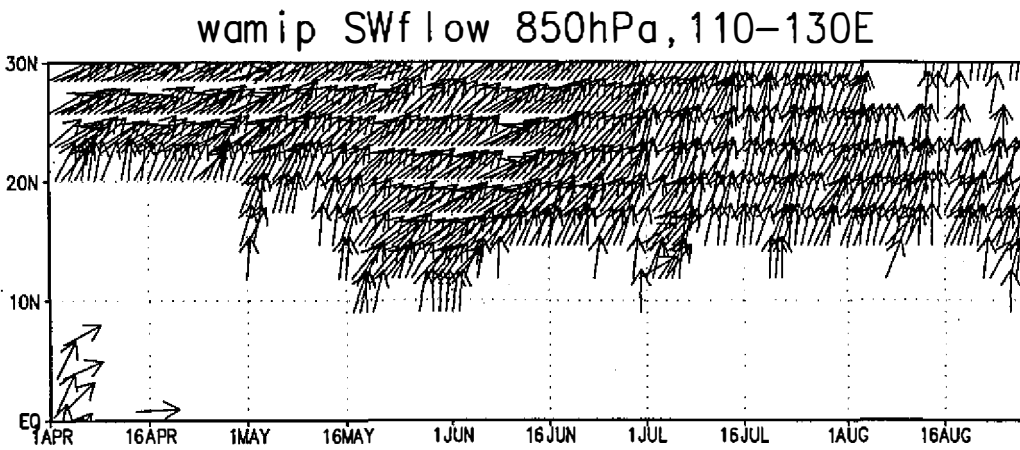


Fig. 26. Simulated climatological-mean of time-latitude section of southwest-westerly wind vector at 850 hPa averaged between 110 °E -130 °E.

East Asia is bordered to the east by the Pacific Ocean and to the southwest by the Tibetan Plateau, which penetrates the middle troposphere. These unique land-sea contrasts and the large-scale topography not only makes the EASM spectacular ( i.e. it last from May to September with precipitation greater than 5 mm/d), but also provides an ideal background to verify the climate model's capability in the EASM simulation.

In this study, we have studied the climatology of the EASM by analyzing the AMIP output data from the NTUGCM, which simulated the robust features of the EASM reasonably well. The NTUGCM has successfully captured the large scale features of the EASM and the sudden changes of monsoon rainfall which are associated with the abrupt changes in large-scale atmospheric circulation. The features captured by this model are:

- (1) A northward progression of the EASM rainfall(Figure18), which is dominated by convective activities.
- (2) A rapid intensification of the lower westerly and upper easterly monsoon circulation as well as the development of the monsoon trough during the period from May to June (Figures13&18 ).
- (3) Three northward jumps of the SH, which over the Western Pacific, assumes a marked seasonal variation in respect to its position. The three northward jumps of the SH during the EASM period are well simulated by the NTUGCM(Figure 20). These are: the first northward jump, which corresponds to the beginning of the rainbelt over the Yangtze and Huaihe River Valleys; the second jump which starts the rainy season in the Yellow River and Huaihe River Valleys, ending in the rainy season of the Yangtze River Valleys; the third northward jump which leads to the beginning of the rainy season in Northern China.
- (4) The northwestward drift of the 200 hPa anticyclone and the development of the cross-equatorial flow (Figs . 21&22).

This study also highlights the simulation of the onset characteristics of the EASM. HC pointed out that the onset of the EASM is characterized by a sudden change in large-scale atmospheric circulation. These features are:

- (1) The development of the low-level cyclonic circulation and the upper-level anticyclone in South Asia,
- (2) sudden eastward retreat of the subtropical Pacific anticyclone at 850 hPa which occupies the SCS in April and early May,
- (3) the 850 hPa wind in the SCS abruptly changes from southeasterly to southwesterly.

Based on the above characteristics, the AMIP simulated mean onset date for the EASM by the NTUGCM is therefore set as 13 May, which is close to the climatological overall mean. From the above discussions, concerning the onset and progression of the EASM, we may confirm that the present model has the ability to simulate the seasonal evolution of the EASM. Thus, the NTUGCM may be a useful tool for understanding the physical mechanisms responsible for the variability of the broad scale EASM.

The present results are encouraging. They indicate that further predictability research on the ASM and long range forecasting of the EASM rainfall may be possible in the near future. However, the present study is just a prelude and there is much work that must be done on the simulation of the EASM. There are four issues which merit future attention:

- (1) The variability of the ASM associated with the Earth's surface forcing involves many complex processes on a variety of time scales. In this study, the model is forced by globally observed SST. We have not discussed the relationship between the monsoon and SST anomalies of the Pacific and Indian Oceans. However, Yang and Lau(1997) pointed out that the impact of SST anomalies on the monsoon is nonlinear with warm and cold events. The change in tropical Western Pacific SST is sometimes important (Soman and Slingo, 1997). There are even more uncertainties in the role of the Indian Ocean in the variability of the Asian monsoon (Palmer *et al.*, 1992; Nigam, 1994; and Soman and Slingo, 1997). Whether the ocean plays an active or passive role in the monsoon and to what extent the ocean influences the monsoon system are unclear. HC pointed out that the orography, land-sea distribution and SST as well as different surface conditions in the Indochina Peninsula and India cannot be neglected during the first transition of the ASM and the onset of the EASM. Therefore, the linkage between the monsoon's variation and surface boundary forcing is very important. In addition, the application of the PBL parameterization scheme is crucial to the model's simulation.
- (2) Although arguments have been put forward to explain this unique event, the cause of the seasonal northward jump of the subtropical high has not yet been clarified. It has been revealed that the seasonal northward jump of the SH concurrently occurs with the abrupt meridional shift, from the south to the north, of the monsoon vertical circulation cell in East Asia. Lin & Miao ( 1981 ) further pointed out that there is a tendency for the change in the mean meridional cell to lead to the northward jump of the SH. The internal dynamics of the SH need more theoretical and numerical studies.
- (3) The dynamic and thermodynamic effect of the Tibetan Plateau is important to the development and maintenance of the ASM. However, in the early stage of the seasonal transition this effect does not function well, because the cold air advection and the adiabatic cooling eliminates the warming caused by the sensible heat flux ( Feng , 1992 ). Theoretical and numerical studies have shown that the upper-level anticyclones can be forced either by a realistic heating distribution (*e.g.* Hoskins and Rodwell, 1995) or by an idealized, deep heating profile (*e.g.* Gill, 1980). The Tibetan Plateau can obviously help establish the upper-level anticyclone and, possibly the first transition of the ASM to some extent, but is unlikely to be the sole and most important factor. HC also pointed out that the heating and lifting effects of the high terrain in the Indochina Peninsula can be more prominent than heating effect of the Tibetan Plateau during the first transition. The exact role of the Tibetan Plateau in maintaining the summer circulation has no unified results yet. Sensitivity studies of the dynamic and thermodynamic effect of the Tibetan Plateau using numerical modeling are needed.
- (4) In view of the fact that the intraseasonal variations are linked to a variety of fundamental physical processes, such as latent heat release (including large-scale and convective heating) and boundary fluxes, a thorough understanding of the phenomenon and better representation of the model physics (such as PBL, cumulus, cloud/radiation, and topography) have a potential impact on the prediction of long-range variations of the tropical and East Asian monsoonal circulations.

**Acknowledgments** The author benefited from discussions with Professors LinHo and H.H.Hsu. Gratitude is also extended to two anonymous reviewers for their helpful comments on the manuscript. This study was supported by the National Sciences Council of the R.O.C., under Grants NSC85-2111-M-022-011-AGT and NSC86-2111-M-002-001-AGT.

## REFERENCES

- Arakawa, A., and Y. Mintz, 1974: The UCLA general circulation model. Notes from a Workshop on Atmospheric Modeling, 25 March - 4 April 1974, Dept. of Meteorology, University of California at Los Angeles, 404 pp.
- Barnett, T. P., L. Dumenil, U. Schlese, E. Roeckner, and M. Latif, 1989: The effect of Eurasian snow cover on regional and global climate variation. *J. Atmos. Sci.*, **46**, 661-685.
- Bhasjar Rao, D. V., K. Yamazaki, and A. Kitoh, 1991: Some GCM experiments of the Asia summer monsoon related to land boundary conditions. *Pap. Met. Geophys.*, **42**, 127-143.
- Boer, G.J., K. Arpe, M. Blackburn, M. Deque, W.L. Gates, T.L. Hart, H. Le Treut, E. Roeckner, D.A. Sheinin, I. Simmonds, R.N.B. Smith, T. Tokioka, R.T. Wetherald, and D. Williamson, 1991: An intercomparison of the climate simulated by 14 atmospheric general circulation models; *CAS/JSC Working Group on Numerical Experimentation*, Report No. 1S, WMO/TD-No. 425.
- Brown, J.A. 1974: On vertical differencing in the sigma system. NMC office note 92, National Meteorological Center, Washington, D. C., 13pp.
- Chouinard, C., M. Beland, and N. McFarlane, 1986: A simple gravity wave drag parameterization for use in medium-range forecast models. *Atmos. Ocean*, **24**, 91-110.
- Ding Yihui, Z. Shenming, and Z. Jian, 1987: A study of the global 200 hPa divergent circulations in the tropics and subtropics in the summer. *Acta Meteorol. Sinica*, **45**, 120-127.
- Ding Yihui, 1994: Monsoons over China. Kluwer Academic Publishers, 419 pp.
- Diimenil, L., and U. Schlese, 1987: Changes to the parameterization package and their impact on perpetual January simulations; In: G. Fischer (Ed.) *Climate Simulations with the ECMWF T21-model in Hamburg. Large Scale Atmospheric Modelling*, Report No. 1, 121-139, Meteorologisches Institut der Universitat Hamburg.
- Feng Zhiqiang 1992: Seasonal variations of the Asian monsoon. Japanese Experiment on Asian Monsoon, 364 pp.
- Finder, J. 1969: A major low-level air current near the Indian Ocean during the northern summer. *Quart. J. Roy. Meteor. Soc.*, **95**, 362-380.
- Gates, W. L., 1992: The atmospheric model intercomparison project. *Bull. Amer. Meteor. Soc.*, **73**, 1962-1970.
- Geleyn, J.-F., 1981: Some diagnostics of the cloud/radiation interaction in the ECMWF forecast model. Proceedings of the Workshop on Radiation and Cloud- Radiation Interaction in Numerical Modeling, European Centre for Medium- Range Weather Forecasts, Reading, England, 135-162.
- Gilchrist, A., 1981: Simulation of the Asia summer monsoon by 11-layer general circulation

- model. Monsoon dynamics. In: J. Lighthill and R. P. Pearce (Eds.), Cambridge University Press, 131-145.
- Gill, A., 1980: Some simple solutions for heat-induced tropical circulation. *Quart. J. Roy. Met. Soc.*, **106**, 447-462.
- Hahn, D., and S. Manabe, 1975: The role of mountains in the south Asia monsoon circulation. *J. Atmos. Sci.*, **32**, 1515-1541.
- He, H., J. W. McGinnis, Z. Song, and M. Yanai, 1987: Onset of the Asian summer monsoon in 1979 and the effect of the Tibetan Plateau. *Mon. Wea. Rev.*, **115**, 1966-1995.
- Hoskins, B. J., and M. J. Rodwell, 1995: A model of the Asian summer monsoon. Part I: The global scale. *J. Atmos. Sci.*, **52**, 1329-1356.
- Hsu, H. H., and C. T. Chen, 1997: Evolution of Large-scale Circulation during the First Transition of Asian Summer Monsoon, (Submitted to Journal Climate.)
- Huang, R.H., 1985: Numerical simulation of the three-dimensional teleconnections in the summer circulation over the Northern Hemisphere, *Adv. Atmos. Sci.*, **2**, 81- 92.
- Ju, J., and J. Slingo, 1995: The Asian summer monsoon and ENSO. *Quart. J. Roy. Meteor. Soc.*, **121**, 1133-1168.
- Kau W. S., H. H. Hsu, A. B. Shei, and K.N. Lion, 1995: The NTU Atmospheric General Circulation Model 1. NTU Technical Report, National Taiwan University, Taipei, Taiwan, 95pp.
- Kitoh, A., and T. Tokioka, 1987: A simulation of the tropospheric general circulation with the MRI atmospheric general circulation model. Part III: The Asia summer monsoon. *J. Meteor. Soc. Japan*, **65**, 167-187. Kitoh, A., 1992: Simulated interannual variations of the Indo-Australian monsoons. *J. Meteor. Soc. Japan*, **70**, 563-583.
- Krishnamurti, T. N., and H. N. Bhalme, 1976: Oscillation of a monsoon system. Part I: Observational aspects. *J. Atmos. Sci.*, **33**, 1937-1954
- Krishnamurti, T. N., and Y. Ramanathan, 1982: Sensitivity of monsoon onset of differential heating. *J. Atmos. Sci.* **39**, 1290-1306.
- Krishnamurti, T. N., 1985: Summer monsoon experiment-A review. *Mon. Wea. Rev.*, **113**, 1590-1626.
- Kuo, H. L., 1965: On formation and intensification of tropical cyclones through latent heat release by cumulus convection. *J. Atmos. Sci.*, **22**, 40-63.
- Lanczos, C., 1966: Discourse on Fourier Series. Hafner Publishing, 255 pp.
- Lau K.-M., and S. Yang, 1997: Climatology and Interannual Variability of the Southeast Asian Summer Monsoon, (To appear in Advances in Atmospheric Sciences.)
- Lau, K-M 1992, East Asia summer monsoon rainfall variability and climate teleconnection. 1. *Meteor. Soc. Japan*, **70**, 211-242,
- Lau, K-M., G. J. Yang, and S. H. Shen, 1988: Seasonal and intraseasonal climatology of summer monsoon rainfall over East Asia. *Mon. Wea. Rev.*, **116**, 18-37.
- Laursen, L., and E. Eliassen, 1989: On the effects of the damping mechanisms in an atmospheric general circulation model. *Tellus*, **41A**, 385-400.
- Lin Benda, and M. Jinhai, 1981: The dynamic analysis of the sudden northward shift of subtropical high at the end of Mei-yu in 1977. *Sci. Atmos. Sinica*, **5**, 255-266.

- Liou, K. N., S. C. Ou, S. Kinne, and G. Koenig, 1984: Radiation parameterization programs for use in general circulation models. Report No. AFGL-TR-84-02171, Air Force Geophysics Laboratory Hanscom Air Force Base, Massachusetts 53pp.
- Liou, K. N., and Q. Zheng, 1984: A numerical experiment on the interaction of radiation, clouds and dynamic process in a general circulation model. *J. Atmos. Sci.*, **41**, 1513-1535.
- Liou, K. N., and G. D. Wittman, 1979: Parameterization of the radiative processes of clouds. *J. Atmos. Sci.*, **36**, 1261-1273.
- Lou, K. N., and S. C. Ou, 1981: Parameterization of the infrared radiative transfer in cloudy atmosphere. *J. Atmos. Sci.*, **41**, 1513-1535,
- Meehl, G. A., 1994: Influence of the land surface in the Asian summer monsoon: External conditions verses internal feedbacks. *J. climate*, **7**, 1033-1049.
- Nakazawa, T., 1992: Seasonal phase lock of intraseasonal variation during the Asian summer monsoon. *J. Meteor. Soc. Japan*, **70**, 597-611.
- Nigam, S., 1994: On the dynamical basis for the Asian summer monsoon rainfall-EL Nino relationship. *J. climate*, **7**, 1750-1771.
- Ou, S. C., and K. N. Liou 1988: Development of radiation and cloud parameterization programs for AFGL global models. Report No. AFGL TR-88-00181, Air Force Geophysics Laboratory, Hanscom Air Force Base, Massachusetts, 88pp.
- Palmer, T. N., C. Brankovic, P. Viterbo and M. J. Miller, 1992: Modeling interannual variations of summer monsoons. *J. Climate*, **5**, 399-417.
- Phillips, N. A. 1975: Application of Arakawa s energy conserving layer model to operational numerical weather prediction. NMC OAice Note 1041, National Meteorological Center, Washington, D. C., 40pp.
- Phillips, N. A., 1979: The Nested Grid Model. NOAA Tech. Report NWS-22, U.S. Department of Commerce, National Oceanic and atmospheric Agency, National Weather Service, Washington, D. C.
- Robert, A. J., 1969: The integration of a spectral model of the atmosphere by the implicit method. Proceedings of the WMO/IUGG Symposium on Numerical Weather Prediction, November 26-December-4, 1968, Japan Meteorological Agency, Tokyo, VII-19-VII-24.
- Roeckner, E., U. Schlese, and B. Rockel, 1989: The impact of cloud and radiation parameterization changes in January and July ~imulations with the ECMWF T21-model; In: G. Fischer (Ed.), Climate Simulations with the ECMWF T21-model in Hamburg. Large Scale Atmospheric Modelling, Report No. 2, 139-186, Meteorologisches Institut der Universitat Hamburg.
- Rosenfield, J. E., M. R. Schoeberl, and M.A Geller, 1987: A computation of the stratospheric diabatic circulation using an accurate radiative transfer model. *J. Atmos. Sci.*, **44**, 859-876
- Shukla, J., 1975: Effect of Arabian sea-surface temperature anomaly on Imdian summer monsoon: A numerical experiment with GFDL model. *J. Atmos. Sci.*, **32**, 503- 511.
- Sela, J., 1980: Spectral modeling at the National Meteorological Center. *Mon. Wea. Rev.*, **108**, 1279-1292.

- Slingo, J. M., and B. Ritter, 1985: Cloud prediction in the ECMWF model. ECMWF TECH. Report No. 46, European Centre for Medium-Range Weather Forecasts, Reading, England, 48 pp.
- Soman, M. K., and J. Slingo, 1997: Sensitivity of Asian summer monsoon to aspects of sea surface temperature anomalies in the tropical Pacific Ocean. *Quart J. Roy. Meteor. Soc.*, **123**, 309-336.
- Sperber, K. R., S. Hameed, G. L. Potter, and J. S. Boyle, 1994: Simulation of the northern summer monsoon in the ECMWF model: sensitivity to the horizontal resolution. *Mon. Wea. Rev.*, **122**, 2461-2481.
- Sperber, K. R., H. Sultan., P. Gerald., and B. James., 1994: Simulation of the northern summer monsoon in the ECMWF model: Sensitivity to horizontal resolution. *Mon. Wea. Rev.*, **122**, 2461-2481.
- Sud, Y. C., and W. E. Smith, 1985: Influence of local land-surface processes on the Indian monsoon: A numerical study. *J. Clim. Appl. Meteorol.*, **24**, 1015-1036.
- Tao Shiyan, X. Suyin, and G. Qiyun, 1962: The characteristics of meridional and zonal types of circulation in East Asia tropics and subtropics in summer. *Acta Meteorol. Sinica*, **28**, 234-247.
- Tao, S.Y., and L.X. Chen. 1985: Summer monsoon in East Asia, Prec. International Conference on Monsoons in the Far East, Tokyo, 5-8 Nov. 1985, 1-11.
- Tao, S., and L. Chen, 1987: A review of recent research on the East Asian summer monsoon in China. In monsoon Meteorology, C.-P. Chang and Y. N. Krishnamurti ed., Oxford Univ. Press, 60-92.
- Tao, S., C. Fu, Z. Zeng, and Q.- Y. Zhang, 1991: Two long-term instrumental climate data bases of the People s Republic of China. Environmental Sciences Division, DOE, Publication No. 3747, ORNL/CDIAC-47, NDP-039, 83 pp.
- Tibaldi, S., T. N. Palmer, C. Brankovic, and U. Cubasch, 1990; Extended-range predictions with ECMWF models: Influence of horizontal resolution on systematic error and forecast skill. *Quart. J. R. Met. Soc.*, **116**, 835-866.
- Wang, W. C., H. H., Hsu, W. S. Kau, X. Z. Laing, Lino, C. T. Chen, A. N. Samel, C. H, Tsou, P. H. Lin, and K. C. Ko, 1996: GCM simulations of the East Asia Climate. East Asia and Western Pacific Meteorology Meteorology and Climate, World Scientific .
- Wang Jizhi, and M. Li, 1982: Cross-equatorial flow from Australia and monsoon over China. *Sci. Atmos. Sinica.*, **6**, 1-10.
- Washington, W.M., R.M. Chervin, and G.V. Rao, 1977: Effects of a variety of Indian ocean surface temperature anomaly patterns on the summer monsoon circulation: Experiments with the NCAR general circulation model. *Pure and App. Grophys.*, **115**, 1335-1356.
- Yamazaki, K., 1988; Influence of sea surface temperature anomalies over the Indian Ocean and Pacific Ocean on the tropic atmospheric circulation -A numerical experiment -. *J. Meteor. Soc. Japan*, **66**, 797-806.
- Yang, S., K. M. Lau, and M. Sankar-Rao, 1996: Precursory signals associated with the interannual variability of the Asian summer monsoon. *J. Climate*, **9**, 949-964.

- Yang, S., and K. M. Lau, 1997: Influences of Sea Surface Temperature and Ground Wetness on Asian Summer Monsoon, (Submitted to Journal of Climate.)
- Yanai, M., C. Li, and Z. Song, 1992: Seasonal heating of the Tibetan Plateau and its effects on the evolution of the Asian summer monsoon. *J. Meteor. Soc. Japan*, **70**, 1B, 319-351.
- Zwiers, F. W. 1993: Simulation of the Asia Summer Monsoon with the CCC GCM-1, *J. Climate*, **6**, 470-486.